esa

ECOSPHERE

CONCEPTS & THEORY

Dual-polarization radar products for biological applications

Phillip M. Stepanian,[1,2,8,]† Kyle G. Horton,[1,3,4] Valery M. Melnikov,[5,6] Dušan S. Zrnić,[5] and Sidney A. Gauthreaux Jr.[7]

[1]*Advanced Radar Research Center, University of Oklahoma, 120 David L. Boren Boulevard, Norman, Oklahoma 73072 USA*
[2]*School of Meteorology, University of Oklahoma, 120 David L. Boren Boulevard, Norman, Oklahoma 73072 USA*
[3]*Oklahoma Biological Survey, University of Oklahoma, 120 David L. Boren Boulevard, Norman, Oklahoma 73072 USA*
[4]*Department of Biology, University of Oklahoma, 120 David L. Boren Boulevard, Norman, Oklahoma 73072 USA*
[5]*National Severe Storms Laboratory, 120 David L. Boren Boulevard, Norman, Oklahoma 73072 USA*
[6]*Cooperative Institute for Mesoscale Meteorological Studies, 120 David L. Boren Boulevard, Norman, Oklahoma 73072 USA*
[7]*Civil and Environmental Engineering, University of Illinois, Urbana–Champaign, 205 North Mathews Avenue, Urbana, Illinois 61801 USA*

Citation: Stepanian, P. M., K. G. Horton, V. M. Melnikov, D. S. Zrnić, and S. A. Gauthreaux Jr. 2016. Dual-polarization radar products for biological applications. Ecosphere 7(11):e01539. 10.1002/ecs2.1539

Abstract. The upgrade of the national network of next-generation weather surveillance radars (NEXRAD) in the United States to dual polarizations has been completed, providing three additional routine data products: total differential phase (ψ_{DP}), differential reflectivity (Z_{DR}), and copolar correlation coefficient (ρ_{HV}). The application and interpretation of these products in the context of aerial bird, bat, and insect movements is an actively developing research front, with potential implications for ecological and conservation studies. The following conceptually derives the definition of these products specifically for NEXRAD weather surveillance radars in the case of biological scatterers. Several cases are presented that illustrate characteristic values and variability of polarimetric quantities for birds and insects, and highlight site-specific differences within the NEXRAD network. Finally, a short prospectus of future directions and applications within the field of polarimetric radar aeroecology is outlined.

Key words: aeroecology; NEXRAD; polarimetry; radar; remote sensing; WSR-88D.

Received 5 April 2016; revised 15 August 2016; accepted 7 September 2016. Corresponding Editor: Brooke Maslo.

[8] Present address: Radar Entomology Unit, Department of Agroecology, Rothamsted Research, West Common, Harpenden, AL5 2JQ, Hertfordshire, UK.
† **E-mail:** phillip.stepanian@rothamsted.ac.uk

Introduction

The national network of weather surveillance radars has been a valuable tool for ecological studies across the United States. Applications have included monitoring broad front migration (Gauthreaux 1971, Gauthreaux and Belser 1998, Diehl et al. 2003, La Sorte et al. 2015*a*, Farnsworth et al. 2016, Horton et al. 2016*b*, *c*), localized bird movements (O'Neal et al. 2010, 2014, Van Den Broeke 2013), roost aggregations (Gauthreaux and Belser 1998, Russell and Gauthreaux 1998, Kelly et al. 2012, Bridge et al. 2015), and stopover sites (Bonter et al. 2009, O'Neal et al. 2010, Ruth et al. 2012, Buler and Dawson 2014, Lafleur et al. 2016) as well as providing observations of bats (Cleveland et al. 2006, Horn and Kunz 2008, McCracken et al. 2008, Frick et al. 2012) and insects (Westbrook 2008, Westbrook et al. 2013). The ability to continuously survey large

expanses of airspace over long periods of time has yielded information on animal abundance (Farnsworth et al. 2004, Horton et al. 2015), distribution (Buler and Diehl 2009, Buler et al. 2012, Buler and Dawson 2014, Bridge et al. 2015), behavior (Diehl et al. 2003, Van Doren et al. 2015, 2016, Horton et al. 2016*b*), and phenology (Frick et al. 2012, Kelly et al. 2012, 2016, Bridge et al. 2015, La Sorte et al. 2015*a*, *b*).

Since the initial deployment of the U.S. Weather Surveillance Radar infrastructure in 1957 (WSR-57), several successive upgrades to the radar network have enhanced sampling capabilities for meteorological observations, yielding mutual benefits for biological applications as well. With each technological advancement comes a period of exploration during which new data must be interpreted within a biological context. The first notable change came with the introduction of Doppler capabilities during the upgrade to the next-generation network of WSR-88D systems (NEXRAD, hereafter; Crum et al. 1993). Prior to this point, only measurements of radar reflectivity factor (Z) were available as standard products. The addition of two new products—Doppler radial velocity (v_r) and spectrum width of radial velocity (σ_v)—required a new paradigm to link these data with biologically meaningful interpretations. Subsequent studies investigated these two Doppler products within the context of biological scattering to interpret their connection to animals aloft (e.g., Gauthreaux and Belser 1998, Liu et al. 2005, Zhang et al. 2005), and they are now commonly used to characterize migratory movements (Gauthreaux and Belser 1998, Diehl et al. 2003, Gauthreaux et al. 2008, Sheldon et al. 2013), calculate traffic rates (Horton et al. 2015, 2016*a*), delineate birds from insects (Gauthreaux and Belser 1998, Fang et al. 2004), and identify roost emergence signals (Russell and Gauthreaux 1998). Similar advances followed the upgrade to super-resolution, which provided greater spatial detail and the ability to resolve fine-scale distributions (O'Neal et al. 2010, Buler and Dawson 2014).

The summer of 2013 marked the conclusion of the most recent upgrade to the NEXRAD network, which now provides dual-polarization measurements to enhance meteorological observations (Doviak et al. 2000). These polarimetric measurements enable delineation among precipitation types (e.g., rain, snow, and hail), provide higher accuracy in quantitative precipitation estimation, and can detect debris signatures that indicate the presence of tornadoes (Ryzhkov et al. 2005, Kumjian 2013*b*). Embedded within all of these applications is the ability of polarimetry to delineate meteorological and non-meteorological signals (Zrnić and Ryzhkov 1999, Ryzhkov et al. 2005), a capability with clear benefits to the ecological research community. Some preliminary biological applications have demonstrated the utility of polarimetric measurements (Zrnić and Ryzhkov 1998, Van Den Broeke 2013, Melnikov et al. 2015, Stepanian 2015, Stepanian and Horton 2015, Horton et al. 2016*b*, *c*, Kelly et al. 2016, Van Doren et al. 2016), but some hesitation still exists among biologists in the widespread adoption of this technology. Two major roadblocks are hindering the transition of polarimetry to biological applications. First, many background texts on polarimetry are written using full mathematical rigor, placing a large emphasis on equations to provide the meaning of polarimetric variables (see the textbook by Bringi and Chandrasekar 2001 for one excellent resource). While those with extensive radar experience may find these descriptions analytically elegant, many others are dissuaded by the overhead required to approach these descriptions. A second major body of work has presented radar polarimetry in an approachable form for meteorologists. These texts provide a physical interpretation of NEXRAD products in terms of hydrometeor types and precipitation processes and are currently the most practical resources for radar biologists (e.g., Rinehart 2010, Kumjian 2013*a*, *b*, *c*). Unfortunately, several major differences between the characteristics and behavior of hydrometeors and airborne organisms result in divergent polarimetric interpretations. Overall, many of the most prolific descriptions of NEXRAD polarimetric products are not suitable for extension to biological scatterers (i.e., birds, bats, and insects).

The goal of this article is to develop an intuitive description of NEXRAD polarimetric products without a reliance on mathematical formulation. This description is not a simplification; the physical processes are illustrated in their full complexity and technical rigor, but rely on graphical illustrations rather than mathematical formulae. Our hope is that step-by-step descriptions will provide an approachable path into radar polarimetry. As

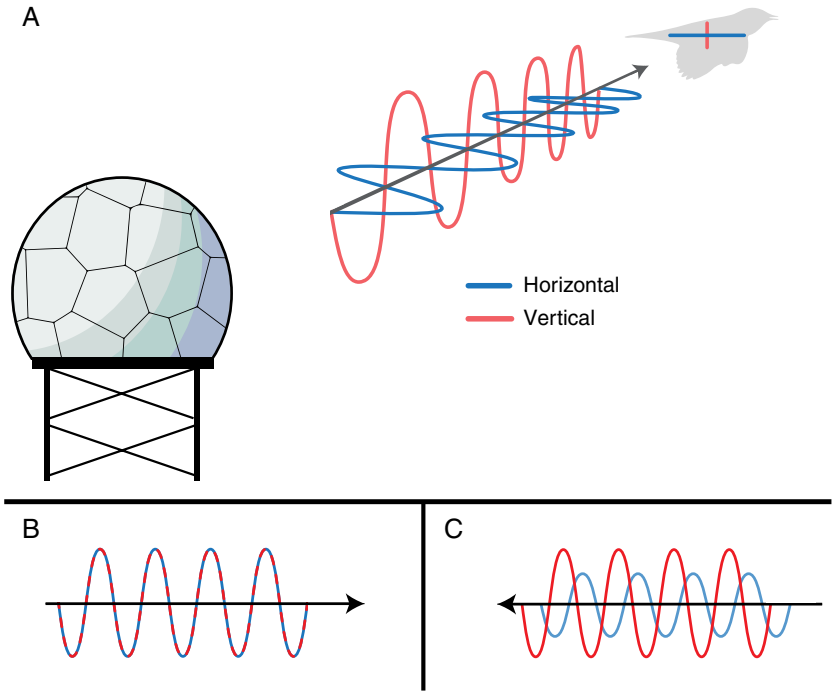

Fig. 1. Wave conventions. (A) A 3-D schematic of a dual-polarization pulse traveling from the radar to a bird. (B) The 2-D convention for illustrating overlaid dual-polarization waves as in (A). (C) The 2-D convention for illustrating non-overlaid dual-polarization waves. In all following cases, the radar will be assumed to be at the left of the schematic and the scatterer will be at the right. Arrowheads indicate the direction of wave propagation.

such, readers should already be familiar with the basic principles of weather radar, and if not, they should see other radar primers first (Eastwood 1967: Chapters 1–3, Diehl and Larkin 2005, Drake and Reynolds 2012: Chapter 15, Larkin and Diehl 2012). The remaining sections are organized as follows: The second section provides an overview of background concepts in electromagnetic propagation and scattering that are relevant for polarimetric radar measurements; the third extends this background to formulate definitions of the three polarimetric products provided by NEXRAD; the fourth illustrates these products and their interpretation in several short case studies; and finally, the fifth section highlights selected prospects and future directions of polarimetric radar studies in ecology.

Background and Terminology

Radio wave basics

It is impossible to describe NEXRAD polarimetric products for biological scatterers without discussing the interactions of electromagnetic (radio) waves, and attempts at doing so result in oversimplifications that invalidate any meaningful interpretation of the data. This necessity usually evokes Maxwell's equations and the associated mathematical baggage attached to formal electromagnetic analysis (see Doviak and Zrnić 1993: Chapter 2, Bringi and Chandrasekar 2001: Chapter 1). As an alternative, we will adopt a graphical approach to visually illustrate wave interactions during propagation and scattering. Herein, we will consider a pulse of electromagnetic radiation emanating from a radar toward a biological scatterer (Fig. 1A). The pulse will contain two waves of orthogonal polarizations: one oscillating in the vertical plane (Fig. 1, red) and the other in the horizontal plane (Fig. 1, blue). To make illustration easier, we will draw these two polarizations on the same plane, using an alternating red-blue dashed line to depict perfectly matched waves (Fig. 1B) and solid lines to show offset waves (Fig. 1C). Herein, the radar will be assumed to be at the left of the schematic and the

scatterer will be at the right. Finally, an arrow will depict the direction of travel of the wave, whether propagating from the radar to the bird (Fig. 1B) or from the bird back to the radar (Fig. 1C).

Electromagnetic waves can be described by a wavelength, amplitude, and phase. Wavelength is the distance between consecutive wave peaks and is ~10 cm for the NEXRAD systems. Related to wavelength is the wave frequency, which describes the rate at which a wave oscillates within a medium (in cycles per second or hertz). Wave amplitude is the maximum height of the wave peaks and depth of the wave troughs. Wave phase is the relative position within the oscillation, that is, peak, trough, or in between, and is measured in units of degrees. The two waves in Fig. 1B have the same wavelength, amplitude, and phase. The waves in Fig. 1C have the same wavelength, but different amplitudes and phases. When multiple waves of similar polarizations occupy the same physical space, they sum coherently to form one resultant wave. Coherent addition refers to combining waves with respect to both their amplitude and phase; that is, the instantaneous collocated wave intensities (and their corresponding signs) get summed to a single intensity for the resultant wave. For example, Fig. 2A illustrates horizontally polarized waves that are in-phase. Because the phases of these waves are matched, the peaks add with peaks, the troughs add with troughs, and the waves interfere constructively to form a resultant wave with greater amplitude. Fig. 2B shows the result of shifting wave #1 by a half wavelength, resulting in waves that are 180° out of phase. As a result, peaks add with troughs creating destructive interference and reducing the amplitude of the resultant wave. This wave shift illustrates a second concept in wave comparison—phase ambiguity. We can see that wave #1 has been shifted by a half wavelength, but we do not know whether it has been shifted forward 180° or backward 180°. Similarly, a forward shift of 270° would look identical to a backward shift of 90°. Additional ambiguity arises when phase shifts are greater than 360°. For example, a forward shift of 361° would look identical to a forward shift of 1°. The combined effect of these processes that result in uncertainty in the interpretation of phase is known as aliasing—an effect most familiar for its role in radial velocity measurements (Doviak and Zrnić 1993: Section 3.6).

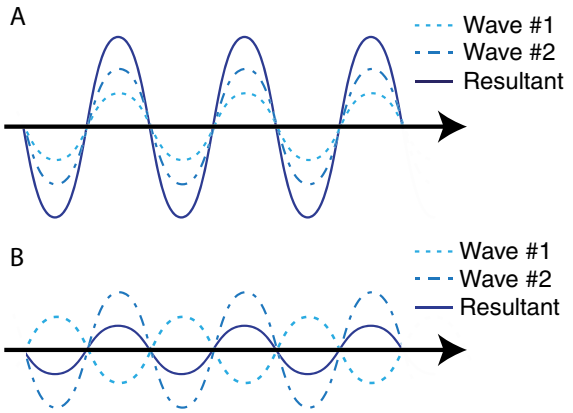

Fig. 2. Coherent interactions between two collocated horizontally polarized waves. (A) Constructive interference of Wave #1 and Wave #2. (B) Destructive interference of Wave #1 and Wave #2.

The Mie curve and resonant scattering

When a transmitted electromagnetic wave interacts with an object, part of the wave is scattered back to the radar. The amount of this incident radiation that is backscattered by the object can be characterized in terms of the object's radar cross section (RCS). The most common RCS characterization was formulated to describe the backscattering area for dielectric (i.e., non-conducting or non-metallic) spheres of a given diameter (Mie 1908). The resulting relation between sphere size and RCS is commonly presented in introductory radar texts as the so-called Mie curve (e.g., Doviak and Zrnić 1993: Figure 3.3, Martin and Shapiro 2007: Figure 2, Rinehart 2010: Figure 4.2, Drake and Reynolds 2012: Figure 4.1, Larkin and Diehl 2012: Figure 13.3). When the physical diameter of a scattering sphere is much smaller than the radar wavelength (e.g., less than 1/16 of the wavelength, or approximately 6.25 mm for NEXRAD), the phase of the wave does not vary much across the physical span of the sphere (Fig. 3A, left). As the wave oscillates in time, the entirety of the sphere produces a single coordinated oscillation that drives the backscattered energy (Fig. 3A, right). When this case of homogeneous oscillation occurs, the RCS of the sphere increases monotonically as a function of the diameter to the sixth power (Doviak and Zrnić

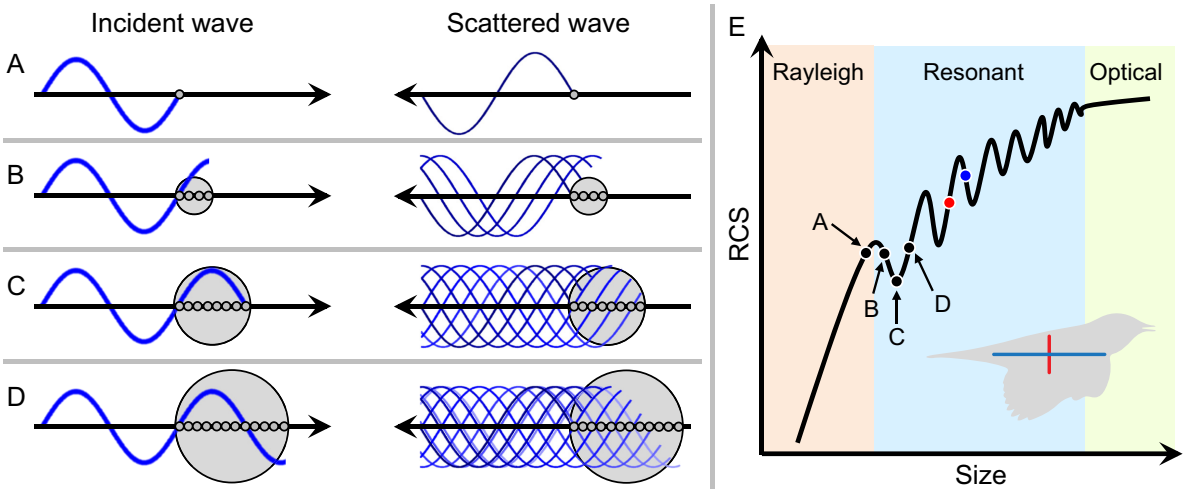

Fig. 3. Resonant scattering from spheres of varying diameters. The left column depicts incident waves, and the right column depicts scattered waves. (A) A sphere within the Rayleigh limit. (B–D) Large spheres conceptualized as a collection of small spheres within the Rayleigh limit. (E) The schematic Mie curve and the RCS values associated with the four spheres, as well as a bird's vertical (red) and horizontal (blue) dimensions.

1993, Section 3.2). More specifically, under these conditions, the energy scattered back to the radar is proportional to the volume of the sphere squared—a condition known as Rayleigh scattering (Fig. 3E). In this Rayleigh scattering regime, RCS has a one-to-one relation with sphere diameter such that a measurement of backscattered power directly corresponds with a specific sphere size. As the size of the sphere increases beyond the Rayleigh limit, different parts of the internal structure of the sphere are exposed to different wave phases (Fig. 3B, left). Conceptually, this large sphere can be thought of as a collection of small spheres for which the Rayleigh condition is valid, with each of these small spheres producing its own backscatter contribution (Fig. 3B, right). Each of these small spheres is exposed to a different part of the wave, causing each to oscillate with a slightly different phase. These uncoordinated oscillations within the body of the large sphere will begin to create a destructive wave component that reduces the overall amplitude of the scattered wave, resulting in the first local maximum of the Mie curve (Fig. 3E). As the sphere continues to grow, this destructive wave component will continue to increase, decreasing the magnitude of the RCS until it reaches a local minimum (Fig. 3C). With an additional increase in size, the spatial configuration of internal oscillations will again create constructive interference and an increase in scattered wave energy (Fig. 3D). This increase in backscattered energy results in a corresponding increase in RCS and the first local minimum of the Mie curve. These oscillations between constructive and destructive wave interference will continue as the size of the sphere continues to increase, resulting in the complex relation between size and RCS known as resonant scattering (Fig. 3E). These resonance effects will continue until the size of the sphere is much larger than the wavelength, such that internal inhomogeneities in oscillations begin to average out to a stable backscattered amplitude—a condition known as geometric or optical scattering (Fig. 3E).

Mie theory is a useful conceptual tool, but is only strictly valid for spheres. For the case of animals, body geometry is not spherical and internal composition is a non-homogeneous distribution of different dielectric materials. Both will result in a divergence from Mie theory. Nonetheless, the phenomenon of resonant scattering illustrated by Mie theory can aid in the interpretation of biological radar signals. For example, all birds and many large insects are above this 6.25-mm size threshold for Rayleigh scattering, making the relation between their size and RCS far from straightforward. Furthermore, because this

threshold is dependent on wavelength, the slight wavelength variation among NEXRAD sites can add an additional degree of freedom to this relationship (Melnikov et al. 2012).

Further complications arise when considering scattering at dual polarizations. The Mie curve is formulated to describe the RCS of spheres, but biological scatterers are decidedly non-spherical. To conceptualize the process of dual-polarization measurements on non-spherical scatterers, it is helpful (although not totally accurate) to visualize each dimension of the scatterer as a separate diameter on the Mie curve (Fig. 3E). In this illustration, it is easy to see that the horizontal polarization is seeing a larger object, resulting in a larger RCS (Fig. 3E, blue), and the vertical polarization sees a smaller object, resulting in a smaller RCS (Fig. 3E, red). If a slightly larger bird of identical proportions were sampled, the resonance effects in each dimension would result in a decrease in horizontal RCS and an increase in vertical RCS. The practical effects of resonant scatter on polarimetric measurements of animals will be discussed in the following sections.

As a final caveat, we should emphasize that a mechanistic understanding of electromagnetic scattering for organisms has still not been attained. For example, while we may conceptualize a bird as a simple homogenous spheroid, it is likely that internal organs have a complicating effect as additional resonant structures with their own interfaces. Similar complications arise from specific details in body shapes and the internal variability in moisture distribution. Simplified conceptual tools like the Mie curve can provide some intuition into scattering processes, but much work is still required until we can fully understand and model these phenomena.

Wave propagation at dual polarizations

For simplicity, we will assume that an electromagnetic pulse propagates unaffected through the clear atmosphere. In actuality, this condition is only strictly true in a vacuum, but we will consider pure air (with an absence of particulates, hydrometeors, or animals) as a close approximation. By this definition, the transmitted radio pulse travels away from the radar at the speed of light in a vacuum, ~300,000,000 m/s. If this pulse suddenly encounters a dense field of spherical water drops (i.e., a cloud), two things will occur: Some of the electromagnetic energy will scatter off of the drops at the edge of the cloud and return to the radar and some of the energy will pass onward into the cloud. This same process will continue through the cloud—some energy will scatter back to the radar, and some will continue forward. This systematic energy loss as the wave passes through the cloud (or any collection of scatterers) is called attenuation (Doviak and Zrnić 1993: Section 3.3). Furthermore, because the refractive index of water is higher than that of clear air, the speed of light is reduced as it travels within the cloud droplets, and the overall forward progress of the wave will be impeded as it passes through the cloud (Doviak and Zrnić 1993: Section 2.2).

These two processes, attenuation and propagation impedance, are sensitive to the dimensions of the drops and the wave polarization. The spherical cloud drops that we have described would affect horizontal and vertical polarizations identically. A cloud of horizontally oriented oblate drops would provide greater scattering in the horizontal polarization, resulting in greater horizontal attenuation. Similarly, these oblate drops would impede the horizontal polarization more than the vertical component, allowing the vertical wave to slowly "outrun" the horizontal. Furthermore, these two propagation effects are dependent on the aerial density (i.e., spatial number concentration) of the scatterers that form the propagation medium. For the case of a single scatterer, the wave energy attenuated and delayed is negligible compared to the energy that passes around the scatterer unaffected. A dense medium would have a much greater effect on the wave energy. That is, for each kilometer the wave travels through the medium, its amplitude is reduced by some number of decibels (dB) and its phase is delayed by some number of degrees. As a result, attenuation and phase delay can be described for each polarization in terms of propagation through a fixed-density medium in units of dB/km and degrees/km, respectively. Several additional quantities are defined that describe the differences in propagation effects between polarizations. The total amount of phase difference that is accumulated as the wave at one polarization outruns the other is the propagation differential phase (Φ_{DP}) in units of degrees. The rate at which the vertical polarization outruns the

horizontal is the specific propagation differential phase (K_{DP}) in units of degrees/km. The difference between the specific horizontal attenuation and vertical attenuation is the specific differential attenuation (A_{DP}) in units of dB/km.

For most cases of biological scatterers in otherwise clear air, the inflight density of individuals is sufficiently sparse that the wave components passing through scatterers are negligible compared with the wave components passing around (and thus unaffected by) scatterers (Zrnić and Ryzhkov 1998). In other words, for radio wave propagation through a flock of birds, the propagation measures of Φ_{DP}, K_{DP}, and A_{DP} are negligible (Zrnić and Ryzhkov 1998, Melnikov et al. 2015). Exceptions may exist when animal densities are exceptionally high, such as during roost, cave, or insect emergences.

Wave scattering at dual polarizations

As the radio pulse impinges upon the body of an organism, the polarized waves excite electromagnetic currents within and across the surface of the animal. The body acts as an antenna as the excited fields are radiated outward from the animal. Unlike raindrops, biological scatterers have complex shapes that result in highly aspect-dependent scattering characteristics. It is sometimes convenient to represent these complicated shapes as equivalent point scatterers. In the same way that the physical body of any object can be reduced to a magnitude (the mass) and location (the center of mass), the scattering characteristics can be summarized as a magnitude (the radar cross section) at a location (the phase center). That is, we can construct a simplified representation of an animal by placing a point scatterer with an equivalent radar cross section at the animal's phase center. Again, because scattering characteristics are polarization specific, we would need equivalent point scatterers for both horizontal and vertical polarizations. Furthermore, the horizontal dimension of an animal's body is typically not identical to the vertical dimension, meaning that the horizontal polarization center of scattering mass (i.e., phase center) is not necessarily collocated with the vertical polarization phase center (Fig. 4A). This phase center offset may vary among species, depending on anatomy and mass distribution (Fig. 4A). As illustrated in Fig. 4B, if a radar transmits

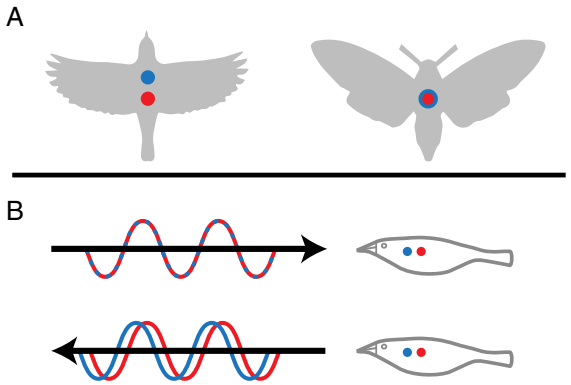

Fig. 4. Phase centers for dual polarizations. (A) Schematic positions of vertical (red) and horizontal (blue) phase centers for a warbler and a moth. (B) Differential phase shift due to scattering.

phase-matched horizontal and vertical waves toward the pictured bird, the horizontal polarization would appear to have scattered first, giving it a head start back to the radar. The resulting backscattered waves would have a phase offset between polarizations. This offset is called the backscatter differential phase (δ) in units of degrees and is related to bird anatomy and incident wave aspect angle.

Perhaps the greatest disparity between the scattering mechanism of raindrops and animals is the significance of an effect called depolarization. When a purely horizontally polarized wave impinges on a raindrop, the wave induces horizontally polarized currents within and across the drop surface. The drop then radiates horizontally polarized waves back to the radar. Describing the raindrop in terms of an antenna, we say that it has high cross-polar isolation. That is, the polarization that is excited, in this case horizontal, is the same polarization that is radiated. Biological scatterers are irregularly shaped, especially compared with spheres and spheroids. When a purely horizontal wave hits an animal, the excited currents that flow along the body can be guided out of the horizontal plane. Portions of these horizontal oscillations become vertical oscillations, which are also radiated from the bird back to the radar (Fig. 5A). As an antenna, the animal has low cross-polar isolation—it does not isolate polarizations, allowing crossover between the horizontal and vertical. For biological scatterers, transmission of a

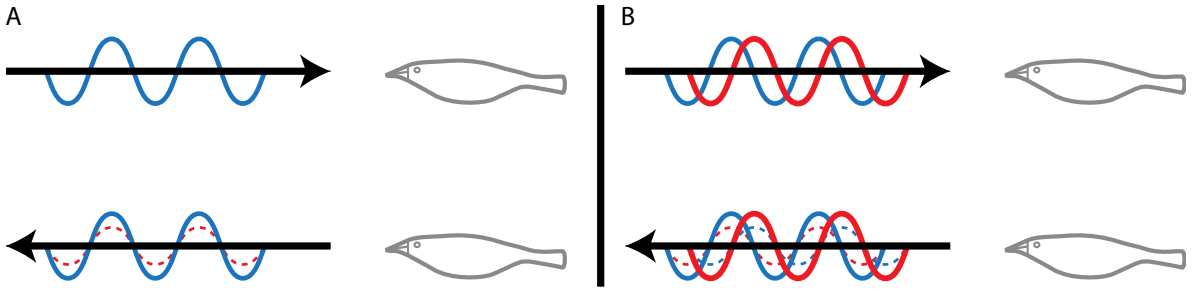

Fig. 5. Effects of depolarization. (A) Decomposition of a horizontally polarized transmitted wave into horizontal (copolar, solid) and vertical (cross-polar, dashed) components upon backscattering. (B) Decomposition of a dual-polarized transmitted wave into two copolar (solid) and two cross-polar (dashed) components upon backscattering.

purely horizontally polarized wave will result in backscatter in horizontal and vertical polarizations (Fig. 5A). Similarly, transmission of a vertically polarized wave will result in backscatter in both polarizations. When describing the backscattered wave components, the term "copolar" indicates the scattered polarization component that is not depolarized (i.e., backscattered horizontal from transmitted horizontal, and backscattered vertical from transmitted vertical). The term "cross-polar" indicates depolarized backscatter components (i.e., backscattered horizontal from transmitted vertical, and backscattered vertical from transmitted horizontal). For a dual-polarized wave having horizontal and vertical polarizations (Fig. 5B), the backscattered wave will have four scattering components: the horizontal copolar (horizontal transmit to horizontal backscatter), vertical copolar (vertical transmit to vertical backscatter), horizontal cross-polar (vertical transmit to horizontal backscatter), and vertical cross-polar (horizontal transmit to vertical backscatter).

Finally, it is typically the case that the transmitted wave pulse will not only interact with a single scatterer, but rather a collection of many individuals. In this case, each individual will separately scatter the pulse as we have just described. Upon reaching the radar, these individual backscatter components will add coherently for each polarization to determine the final received signal amplitudes and phases. As a result, the final received signal will often be dominated by larger scatterers (in the RCS sense). For example, the measured signals for a sampling volume containing a single large oblate spheroid would be approximately the same if a small sphere were also in the volume because the addition would be dominated by the high-amplitude signal contribution (Fig. 6). Similarly, backscattered signals with different phases will sum such that the final phase is influenced more by the signal with greater amplitude. Overall, measurements of volumes containing multiple scatterers are likely often biased toward the characteristics of the largest scatterers.

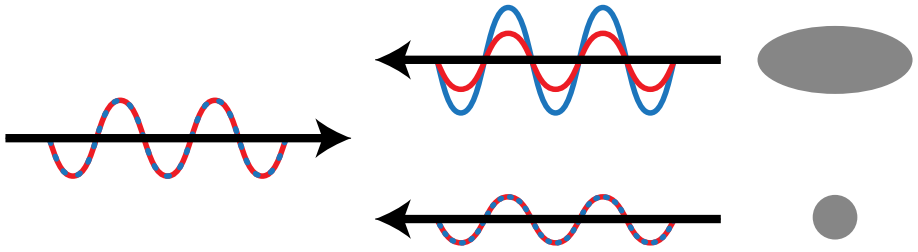

Fig. 6. Backscatter contributions from two scatterers (a large oblate spheroid and a small sphere) for a transmitted dual-polarized wave in initial phase alignment.

In summary, each organism in a resolution volume yields four backscatter contributions, two copolar and two cross-polar. The final received signal is the sum of every individual's contribution within that polarization. The logarithmic ratio of the final received powers at horizontal and vertical polarizations is the differential reflectivity (Z_{DR}) in units of dB. The difference in final received phases between the horizontal and vertical polarizations is the measured differential phase (ψ_{DP}) in units of degrees. The ensemble similarity between measurements at these two polarizations is reported as the copolar correlation coefficient (ρ_{HV}). The precise definitions and interpretations of these three products are presented in the following section.

NEXRAD Dual-Polarization Products

Modes of transmission and reception

Prior to the dual-polarization upgrade, NEXRAD systems transmitted and received in purely horizontal polarizations. As a result, the effects of biological depolarization had little practical significance; some of the horizontal transmission returned in a vertical polarization, but the lack of vertical reception meant that these signals were not detected. During this time, some studies using non-operational dual-polarized research radars produced polarimetric observations of biological scatters that revealed their spatial patterns across a horizontal domain (i.e., in plan-position indicators, PPIs). Two studies (Mueller and Larkin 1985, Lang et al. 2004) showed azimuthally symmetric patterns in fields of Z_{DR} for migrating insects in strong directional alignment, demonstrating the dependence on aspect angle for these measurements. The axis of symmetry in these radar fields was coincident with the axis of insect body symmetry such that radar measurements of the left side of a collection of aligned insects were a mirrored reflection of measurements of the right side. Similar symmetric azimuthal dependence in Z_{DR} and ψ_{DP} was observed for migrating birds (Zrnić and Ryzhkov 1998). In each of these cases, mirrored symmetry of Z_{DR} values revealed a head–tail axis indicative of common orientation—a result that also appeared in polarimetric measurements abroad (Rennie et al. 2010). Following the NEXRAD upgrade, polarimetric measurements from WSR-88D systems yielded confounding results (Van Den Broeke 2013, Melnikov et al. 2015, Stepanian and Horton 2015). In NEXRAD observations, most notably for migrating birds, Z_{DR} did have strong azimuthal dependence, but was often non-symmetric.

The source of this disparity is the methods used by the radar systems to transmit and receive dual polarizations. The former studies used radar systems that alternated between transmitting and receiving single-polarization pulses (e.g., CSU-CHILL radar: Mueller and Larkin 1985, Lang et al. 2004; NSSL Cimarron Radar: Zrnić and Ryzhkov 1998; UK Thurnham radar: Rennie et al. 2010). As a result, depolarized wave contributions were not detected by the radar receiver. Conversely, NEXRAD operates in a simultaneous transmission and reception (STAR) mode, sending a mixed polarization pulse and receiving all wave contributions. One benefit of STAR operation is that one pulse can return dual-polarization information, as opposed to two pulses, effectively doubling the radar's sampling rate (Ryzhkov et al. 2005). As discussed earlier, meteorological scatterers have very little depolarization and typically return negligible cross-polar signals. As a result, meteorological signals look similar in STAR operation as they would in alternating mode. The same is not true for biological scatterers (Melnikov et al. 2015), as will be demonstrated in the following sections. An additional description of polarimetric radar modes of transmission and reception (as well as the associated variables) is presented by Drake and Reynolds (2012, p. 381).

Total measured differential phase (ψ_{DP})

One product provided by NEXRAD is the total measured phase difference between horizontal and vertical polarizations (ψ_{DP}). As discussed in the previous section, dual-polarization phases in initial alignment can be modified independently by propagation through a medium (the Φ_{DP} contribution) or scattering off of a non-spherical object (the δ contribution; Fig. 4). While it is conceptually convenient to visualize waves in initial alignment, NEXRAD systems do not control the polarization phases upon transmission, and therefore, there is an initial phase offset in the transmitted waves (ψ_t). Because this offset can be caused in part by slight differences in radar

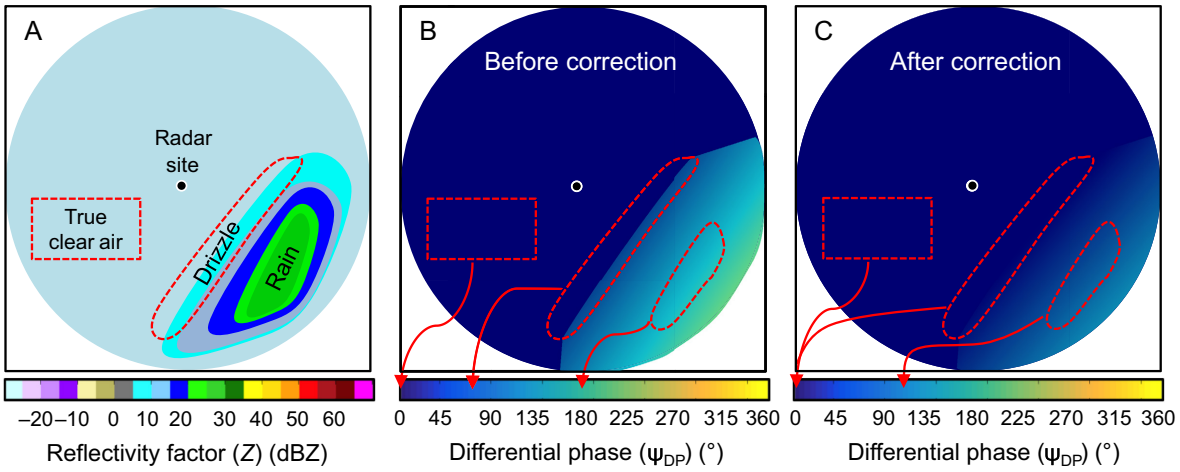

Fig. 7. Schematic demonstration of correction of differential phase in light rain. (A) Field of reflectivity factor indicating rain to the southeast of the radar site. (B) Original field of differential phase showing values at edge and center of rain shower. (C) Corrected field of differential phase.

hardware (e.g., waveguide length and wavelength), the differential phase upon transmission varies among NEXRAD sites and is generally not known. Similarly, the received waves must travel through the radar hardware before they are digitized and recorded, yielding additional phase shifts upon reception (ψ_r). Again, this offset is site specific, can be positive or negative, and is not generally known. Furthermore, the phase shift upon reception is not necessarily related to the phase offset at transmission, leading to two independent sources of differential phase within the radar hardware. With these effects in mind, the total measured differential phase is the sum of the initial differential phase upon transmission (ψ_t), the propagation phase shift while traveling to the scatterer (i.e., the first half of the total propagation path, $0.5\,\Phi_{DP}$), the phase shift due to scattering (δ), the propagation phase shift while returning to the radar (i.e., the second half of the total propagation path, $0.5\,\Phi_{DP}$), and the phase shift upon reception (ψ_r) such that:

$$\psi_{DP} = \psi_t + 0.5\,\Phi_{DP} + \delta + 0.5\,\Phi_{DP} + \psi_r \quad (1)$$

and is reported as a value between 0° and 360° (Melnikov et al. 2015). In meteorological applications, this value is interpreted as the degrees that the horizontal wave lags the vertical wave. In biological applications, it is possible that the vertical wave may lag the horizontal wave, resulting in a negative phase offset. Because of phase aliasing, such an offset of −90° would be reported as +270°, leading to ambiguity in the magnitude and direction of the shift.

Remembering that the propagation contribution through biological scatterers yields negligible phase shifts, the total measured differential phase can be reduced to the contribution from the radar system (the combination of transmission and reception) and the phase shift due to the scatterer. While the individual system contributions are unknown, their summed effect can be found in special situations. Light rain showers contain tiny near-spherical drizzle drops with negligible differential phase shifts from scattering (Fig. 7A). When such showers are located near the radar (5–30 km; ROC 2014) with clear air in between, the only initial source of phase differential is from the radar system itself. The value of ψ_{DP} measured on the edge of the rain shower in this situation is equal to the sum of the system phase shifts upon transmission and reception (Fig. 7B). As the beam propagates farther into the rain, additional phase shifts from propagation can accumulate (Fig. 7B). By inspecting the lightest drizzle on the edge of the rain shower, the ψ_{DP} in this region can be identified and subtracted to remove this system contribution (Fig. 7C). Following this procedure, Eq. 1 can be simplified to $\psi_{DP} \approx \delta$, thereby relating the subsequent radar measurements of airborne animals directly to a single scattering

characteristic of the sampled group of organisms. In an effort to standardize ψ_{DP} data among radar sites, the NEXRAD Radar Operations Center has chosen an initial system differential phase value of 60° as a calibrated standard for all sites (ROC 2014).

It is worth noting that many real-time radar visualization tools do not display the differential phase product (in degrees), but rather its range derivative, specific differential phase (K_{DP}, in degrees/km). Because this product is designed for propagation through meteorological scatterers, it often censors biological signals in quality control, providing no data in the cases of aerial animal movements. As an alternative, archival data with a lag of several days can be downloaded from the National Centers for Environmental Information (NCEI; formerly the National Climatic Data Center, http://www.ncdc.noaa.gov/data-access). These data files do contain the total measured differential phase product and can be plotted using the National Oceanic and Atmospheric Administration's Weather and Climate Toolkit (http://www.ncdc.noaa.gov/wct/). Similarly, up-to-the-minute data can now be downloaded through the latest version (4.0.1) of the Weather and Climate Toolkit using the Amazon Web Services site (https://aws.amazon.com/noaa-big-data/nexrad/).

Differential reflectivity (Z_{DR})

Prior to the NEXRAD upgrade to dual polarizations, radar reflectivity factor (Z) was reported for the horizontal polarization only, providing information related to the number concentration (i.e., aerial density) of scatterers and their size in the horizontal dimension. At dual polarizations, reflectivity factor can be measured for both horizontal and vertical wave contributions and is often related to the size of scatterers in each polarization dimension. Taking the ratio of the received wave powers at each polarization yields the differential reflectivity (Z_{dr}) in linear units. It is customary to take the logarithm of this value, that is, $10\log(Z_{dr}) = Z_{DR}$ in decibel units, and call it simply differential reflectivity. This is natural because the reflectivity factor is also expressed in logarithmic units of dBZ. Using transformation rules for logarithms, this differential reflectivity (Z_{DR}, in units of dB) can be defined as the difference between the measured radar reflectivity factor in the horizontal polarization (Z_H, in dBZ) and the vertical polarization (Z_V, in dBZ):

$$Z_{DR} = Z_H - Z_V. \quad (2)$$

Because the number concentration (i.e., aerial density) of animals in the airspace is identical for measurements at both polarizations, its contribution to each reflectivity factor term in Eq. 2 is identical. Thus, the effect of number concentration subtracts away and does not affect the final differential reflectivity value. As a result, Z_{DR} only depends on the radar cross section of the sampled organisms at each polarization. For many meteorological scatterers and for wavelengths much larger than the scatterer size, this value is directly related to the physical shape (i.e., aspect ratio) of the measured scatterers such that large positive values of Z_{DR} indicate horizontally oriented oblate objects, large negative values indicate vertically oriented prolate objects, and values near zero indicate spheres or collections of randomly oriented particles (Rinehart 2010, pp. 208–212). This simple interpretation does not generally hold true for biological scatterers, with deviations stemming from several causes.

As discussed in previous sections, the RCS of a scattering object at a defined polarization depends on the size of the object in that dimension. For scatterers that are large as compared to the radar wavelength (i.e., greater than 6.25 mm), the RCS does not monotonically increase. For large non-spherical scatterers such as birds, bats, and large insects, resonance affects each polarization independently. The result of these different resonance effects is that a wide range of Z_{DR} values can represent a single physical aspect ratio. The schematic Mie curve in Fig. 3E can provide a simple illustration of this process of differential resonance. The schematic bird in the figure has body dimensions in the horizontal and vertical polarization planes (blue and red lines, respectively). Following the Mie curve, these body sizes correspond with an RCS value for the horizontal and vertical polarizations (blue and red points, respectively). If we assume the difference between the horizontal and vertical RCS of the bird—their vertical separation on the Mie curve—is a proxy for Z_{DR}, we can see that slightly increasing the size of the bird while maintaining the same aspect ratio will result in an increase in

vertical RCS (red) and decrease in horizontal RCS (blue), yielding a lower value of Z_{DR}. Similarly, if the size of the bird were slightly decreased while maintaining the same aspect ratio, the vertical RCS (red) would decrease, whereas the horizontal RCS (blue) would increase, resulting in a higher Z_{DR}. Clearly, for most animals, there is not a simple relationship between Z_{DR} and physical aspect ratio.

Not only does the RCS of an object depend on its size in that dimension, but it is also dependent on the precise wavelength of the radar system. Thus, slight variations in the transmitted wavelength can result in slight variations in RCS in each polarization. In order to avoid radio interference among neighboring radar sites, the NEXRAD network uses slightly different radar wavelengths at nearby sites. Melnikov et al. (2012) showed that this slight variation in wavelength (10.0 cm vs. 11.1 cm) can result in Z_{DR} variations ranging from +10 dB to −5 dB for identical bird-like scatterers.

An additional complication of Z_{DR} measurements in the STAR configuration is the effect of cross-polar contributions to the final measured value. As illustrated in Fig. 5A, single-polarization transmissions will result in dual-polarization signals upon scattering in the case of biological organisms. When dual polarizations are transmitted simultaneously, the result of scattering is four polarization contributions—two copolar and two cross-polar (Fig. 5B). Because the dual-polarization signals are received simultaneously, the received horizontal reflectivity factor (Z_H) is really the coherent sum of the copolar horizontal scattering contribution (Z_{HH}) and cross-polar (i.e., vertical-to-horizontal) scattering contribution (Z_{HV}). The same effect is true in the received vertical polarization such that the received vertical reflectivity factor (Z_V) is the coherent sum of the copolar (Z_{VV}) and horizontal-to-vertical depolarized (Z_{VH}) wave contributions. Because copolar and cross-polar contributions add coherently, and the two copolar waves do not necessarily have the same phase, the cross-polar contributions affect each copolar backscatter wave differently. The result is a dependence of Z_{DR} on cross-polar wave contributions and the phase at which these contributions are offset (Ryzhkov and Zrnić 2007).

Unfortunately for biological applications, storage of Z_{DR} data has been optimized for typical meteorological phenomena and spans from approximately −8 dBZ to +8 dBZ. More precisely, the largest value that can be reported is +7.9375 dBZ and the smallest is −7.875 dBZ. Any measurements that exceed these limits are reported as these values exactly. For example, if the radar measured a Z_{DR} value of −10 dBZ, it would be recorded as −7.875 dBZ. Similarly, measurements of 10, 11, or 20 dBZ would all be recorded as 7.9375 dBZ. When considering frequency histograms of Z_{DR}, the ultimate effect is that the "tails" of the distribution that are outside of the −7.875 dBZ to +7.9375 dBZ range are "clipped" and recorded as those maximum values exactly. The result would be spikes in the histogram at these extrema where measurements saturated the available dynamic range of values. Such a case is presented in the following section.

When visualizing Z_{DR} images on most software packages, the colorscale is often optimized for the expected meteorological observations with positive values using a rainbow colorscale and negative values using a grayscale. This configuration can have the effect of emphasizing the presence of positive Z_{DR} values in the image, while lowering the apparent range of negative values.

Copolar correlation coefficient (ρ_{HV})

The final electromagnetic waves that are recorded by the radar receiver are a complex combination of effects from propagation through the atmosphere, scattering by collections of organisms, and variations within the radar hardware itself. These effects result in changes in the amplitude and phase of the measured signals at each polarization. In some cases, these processes have an equal effect on waves at both polarizations, while other times the signals at each polarization are affected differently. With this variability in mind, it is useful to consider the overall similarity of the received waves at the two polarizations. More specifically, we can compare the two waves by calculating the correlation between the two polarized waves.

There are a few names for this coefficient used interchangeably in the literature including the cross-correlation coefficient (Ryzhkov et al. 2005), copolar correlation coefficient (Bringi and

Chandrasekar 2001, p. 132, Drake and Reynolds 2012, p. 382), copolar cross-correlation coefficient (Zrnić et al. 2006), or simply, correlation coefficient (Doviak and Zrnić 1993: Section 6.8.5). The magnitude of this correlation coefficient between copolar channels at a time offset of zero (denoted $|\rho_{HV}(0)|$ or simply ρ_{HV}; unitless) for each resolution volume depends on the similarity of the received signals at the two polarizations across multiple pulses. The backscattered signal characteristics are a function of the aspect ratio and phase centers of organisms within the volume. By aspect ratio, we mean the true geometric aspect ratio or shape within the Rayleigh region, and the Mie aspect ratio equivalent otherwise.

For a sampling volume containing stationary scatterers, there is no pulse-to-pulse variation caused by scatterers and ρ_{HV} has a value of 1. If the motion, shape, or orientation of scatterers becomes more variable, the signals at each polarization will become less correlated and ρ_{HV} will decrease (Sachidananda and Zrnić 1985, Doviak et al. 2000). Similarly, this value will decrease when scatterers are inhomogeneously dispersed within the sampling volume—an effect known as non-uniform beam filling (Ryzhkov 2007, Kumjian 2013*c*). Unlike raindrops, the shape, body position, orientation, and spatial distribution of animals are highly variable, resulting in intrinsically lower values of ρ_{HV}. Furthermore, the physical act of flying results in substantial changes in body geometry through wing flapping and flexing that can change backscattering characteristics (i.e., RCS and phase centers at each polarization). Again, these scattering mechanisms and their variation with animal body position are still a subject of ongoing research.

As was discussed with the storage of Z_{DR} data, the available range of ρ_{HV} values has been selected to accommodate typical meteorological scatterers. Because most precipitation has correlation coefficient values near 1, the minimum reportable value by NEXRAD has been set to 0.20833. If a biological scatterer produces a correlation coefficient lower than this value, it will be reported as this value exactly. Similarly, while it is possible to get ρ_{HV} values above 1 due to statistical artifacts, these measurements are limited to 1.05166. Again, the practical result in terms of ρ_{HV} histograms is a clipping of the tails beyond these values, and frequency spikes at these two extrema.

As with the other polarimetric products, the colorscale for correlation coefficient in most plotting software packages has been designed for viewing weather phenomena. As a result, most color variation is contained above 0.9 with poor dynamic range of colors below 0.85. When visualizing correlation coefficient using these packages, it is worth noting that small variations at high magnitudes (e.g., 0.95 vs. 0.97) will appear much more significant than large variations at small magnitudes (e.g., 0.2 vs. 0.5).

Textures of polarimetric fields

Finally, with the addition of these three polarimetric products comes the ability to analyze their local spatial characteristics, namely their texture. The texture of a radar product at a given pixel is typically defined by some statistical measure of variability (e.g., standard deviation, variance, root-mean-square deviation) of the surrounding pixel values (Chandrasekar et al. 2012). The pixels included in this calculation may span various regions in range, azimuth, or both. Polarimetric textures are related to the variability in the identity and behavior of organisms within and across resolution volumes. For example, when the composition of sampling volumes is heterogeneous, adjacent volumes will have different polarimetric characteristics and therefore high spatial standard deviations. High standard deviations can still occur in the cases of homogeneous species compositions if behavior differs. For example, two adjacent volumes may both contain the same bird species, but if one collection is being viewed head-on while the other is side-on, the volumes will have different values of Z_{DR} and higher Z_{DR} textures.

The texture of a polarimetric quantity will vary as a function of distance from the radar, with lower textures at farther ranges (Gourley et al. 2007). As the width of sampling volumes increases with range, they each encapsulate more scatterers and higher intravolume variability. The overall effect of this increase in spatial sample size is a better representation of the average characteristics of scatterers in the airspace, which results in lower variation between sampling volumes. When using texture measures for characterizing scatterers, it is often necessary

to normalize these measures in range to avoid this effect (Gourley et al. 2007). Two examples of the utility of polarimetric texture parameters for NEXRAD biological identification have been shown for the root-mean-square deviation of ψ_{DP} in range (Ryzhkov et al. 2005, Park et al. 2009) and the variance of Z_{DR} in both range and azimuth (Lakshmanan et al. 2015). Presently, texture parameters are not provided as NEXRAD data products or calculated in plotting software packages, thus requiring ad hoc computer codes to compute and visualize these quantities.

Cases of common alignment

The mutual alignment of organisms' headings (or lack thereof) will affect dual-polarization measurements. Unlike most meteorological scatterers, airborne organisms are not rotationally symmetric around a vertical axis; that is, the appearance of an individual is dependent on the angle from which it is observed, whether head-on, tail-on, or side-on. This effect on single-polarization measurements has been well documented, with manifestations of a "dumb-bell" pattern of reflectivity factor in azimuth during the widespread alignment of birds and insects (Diehl and Larkin 2005, Drake and Reynolds 2012, p. 140). Aside from these broad front migratory movements, alignment also occurs on localized scales during roost or cave exoduses by colonies of birds or bats, as well as organized dispersive movements over shorter distances. In these cases, alignment is deduced by the variation in polarimetric quantities with respect to view angle (Van Den Broeke 2013, Melnikov et al. 2015, Stepanian and Horton 2015).

Conversely, some flight behaviors, such as aerial foraging or soaring, yield headings with little or no common alignment. Often, these disorganized flights correspond with highly directional radial velocity fields, yielding the incorrect assumption that movements are coordinated over a large scale. In actuality, these patterns result from the background wind field—in which all flight is embedded—producing organized ground speed directions (i.e., tracks) despite haphazard headings. These cases are characterized by relatively homogeneous polarimetric fields that do not vary with view angle.

Finally, the intermediate case exists when organisms assume a weak alignment, or mixtures of taxa align differently. In these cases, polarimetric fields may show a slight variability in view angle, with large magnitudes "averaging out" from the variation in view angles within each sampling volume. In other cases, especially when multiple taxa are present, the polarimetric fields may represent the organisms with the larger reflectivity contribution (as in Fig. 6). For example, at similar aerial densities, the polarimetric quantities of northward-migrating waterfowl will dominate those of westward-migrating moths.

Interpreting NEXRAD Images

With the polarimetric products defined, the final task is to relate these concepts to NEXRAD images of biological activity. Four cases illustrate much of the range of biological signatures commonly observed by NEXRAD and will compare first the variability of polarimetric fields among taxa and flight behavior and second the site-specific differences caused exclusively by the radar system. For each case, archival Level II data have been downloaded from the NCEI data access web system (http://www.ncdc.noaa.gov/data-access) and plotted using custom MATLAB software and colorscales.

Fig. 8 shows a snapshot of the airspace surrounding the Huntsville, Alabama radar (KHTX), on 11 August 2015 at 11:15 UTC (06:15 CDT; 10 min after local sunrise) from the 0.5° elevation angle. The upper panels show the original three NEXRAD spectral moments: radar reflectivity factor (left), Doppler radial velocity (center), and spectrum width of radial velocity (right). The middle row shows the three polarimetric products: differential reflectivity (left), measured differential phase (center), and copolar correlation coefficient (right). To better accommodate the expected phase shifts from biological scatterers, the differential phase values between 270° and 360° have been shifted backward by 360° to span the range of −90° through 0°. The bottom row shows two polarimetric texture parameters: the variance of Z_{DR} in a 5 × 5 pixel neighborhood (left; Lakshmanan et al. 2015) and the root-mean-square deviation of ψ_{DP} over 9 pixels in range (center; Park et al. 2009). Additionally, a manually annotated schematic of the airspace overviews the identity of scatterers and their motions (right).

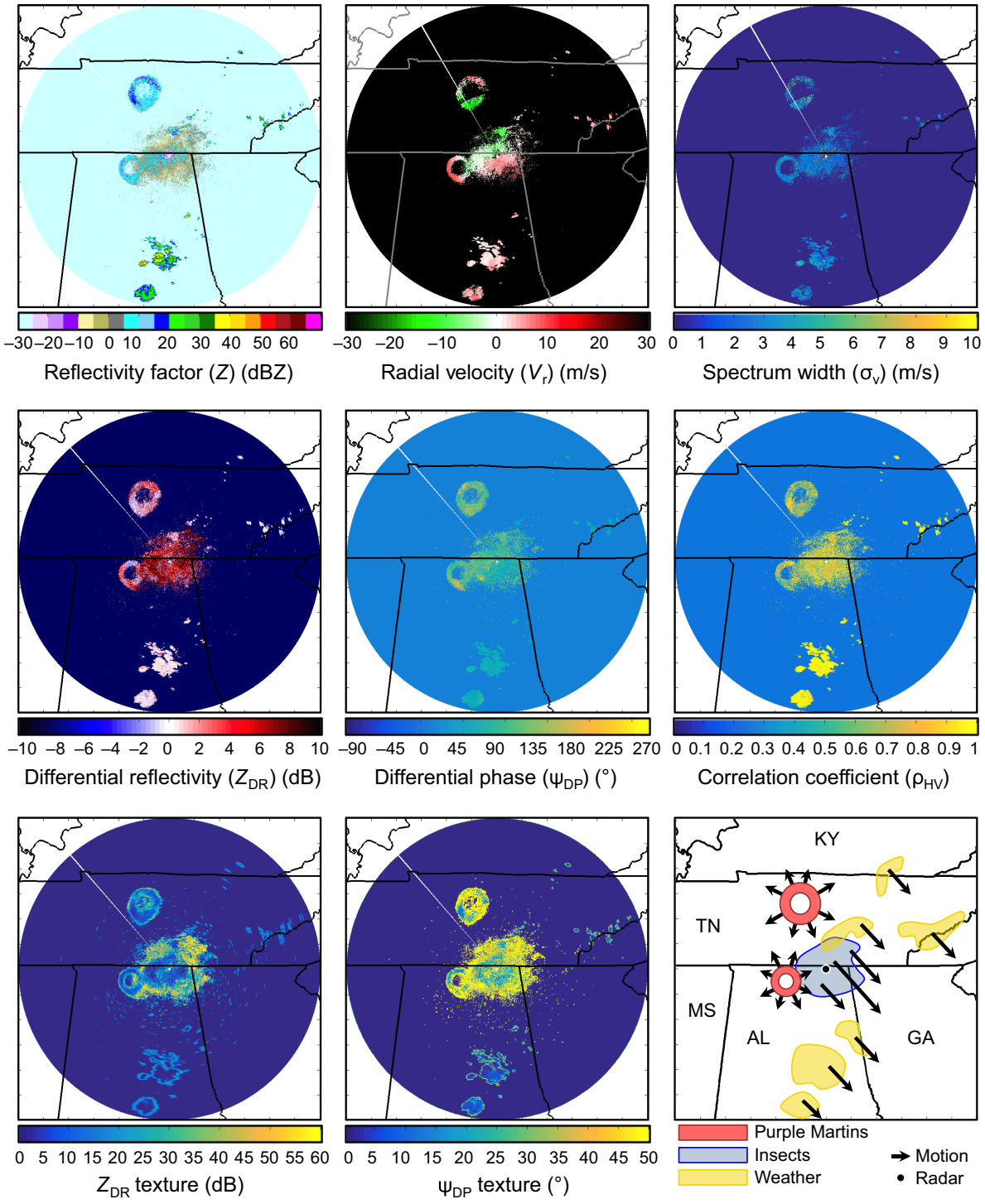

Fig. 8. Radar products for the Huntsville, Alabama NEXRAD radar (KHTX) on 11 August 2015 at 11:15 UTC for the 0.5° elevation angle. Map domain is 600 km by 600 km.

Three notable signals occur during this snapshot. First, two colonies of Purple Martins (*Progne subis*) are engaged in their morning roost exodus, evident from the divergence signatures in radial velocity (Russell and Gauthreaux 1998). Aside from the characteristic radar signatures and phenological timing, the presence and identity of these roosts have been validated on the ground by observers from the Purple Martin Conservation Society (www.purplemartin.org). The organized alignment directed outward from the roost provides radar observations of the birds across the full range of view angles. The effect of this alignment manifests as variations in polarimetric quantities around the circumference of the exodus ring. The range of Z_{DR} in both roosts reaches a minimum value below −4 dB. Naïve interpretation might suggest that these regions of birds are banking, climbing steeply, or otherwise engaging in flight behavior that make them more vertically oriented; however, we know that these negative Z_{DR} values are only an effect of wave resonance. Similarly, one should not assume that the variations in polarimetric characteristics around the roost ring indicate a variation in taxa, because in this case we can conclusively state that there is only one dominant species in the ring.

The second major group of scatterers in the image appears to be insects. Using their collective ground speeds (via analysis of v_r) and wind speeds from the 12 UTC balloon sounding at the Nashville, TN weather forecast office, the airspeed of the scatterers can be calculated by vector subtraction (see Stepanian and Horton 2015 for discussion and caveats on this calculation). In this case, the mean airspeed over the region is 1.80 m/s, further supporting the dominant presence of insects (Appendix S1). The apparent concentration of insects around the radar site indicates their presence at lower altitudes that are sampled near the radar, with the majority of signals originating under 300 m above the ground level. The values of Z_{DR} associated with these insects are generally higher than for the Purple Martins and suggest weak quasisymmetric lobes of values that saturate the +8 dB threshold (oriented WSW to ENE). Combined with the radial velocity pattern associated with the insects, it is likely that the insects are weakly aligning with a southeastward wind.

The final radar signatures appearing at this time are a collection of scattered rainstorms. These are most easily identified by ρ_{HV} near 1, Z_{DR} near 0 dB, and ψ_{DP} near the system calibration offset of 60°. Note that one small storm overlays the insect signals to the north of the radar site and produces polarimetric values that are between those of pure insects and pure rain. The radial velocity associated with the storms shows the environmental flow direction toward the southeast, reinforcing our conclusions that insects are reacting to the surrounding wind field.

By manually annotating the identity of scatterers in the radar image, it is possible to analyze characteristic ranges of polarimetric values for different scatterer types. Fig. 9 shows normalized frequency histograms for the radar fields in Fig. 8, which have been separated by scatterer type using the annotation shown in the lower-right panel of Fig. 8. Frequency histograms provide the ability to quickly compare the modes and variability of these three scatterer types (Fig. 9). In this specific case, the three types each have a distinct mode in reflectivity factor, with insects having the lowest values and weather having the highest. Both types of biological scatterers have more variation in radial velocity values than weather, and the distributions of spectrum width show the typical increase associated with birds (Fang et al. 2004, Gauthreaux et al. 2008). The histograms of differential reflectivity show characteristic weather values near 0 dB and generally positive biological values that span the entire dynamic range. At both ends of the Z_{DR} distribution, biological values exceeding the ±8 dB limits have been clipped, resulting in spikes at these extrema. This effect is most notable for the insects, which have a Z_{DR} mode near 6 dB and much of the distribution outside of the maximum resolvable limit. Values of differential phase for weather are near the calibration standard of 60°, and there is a clear difference in the modal values for birds and insects. As expected, correlation coefficient is approximately 1 for weather signals, with lower values for both insects and birds. Overall, the histograms of polarimetric variables are broader for biological scatterers as compared to meteorological signals, in part because of their high variability in scattering characteristics depending on viewing angle. When considering spatial variability of the polarimetric variables, texture fields of Z_{DR} are much

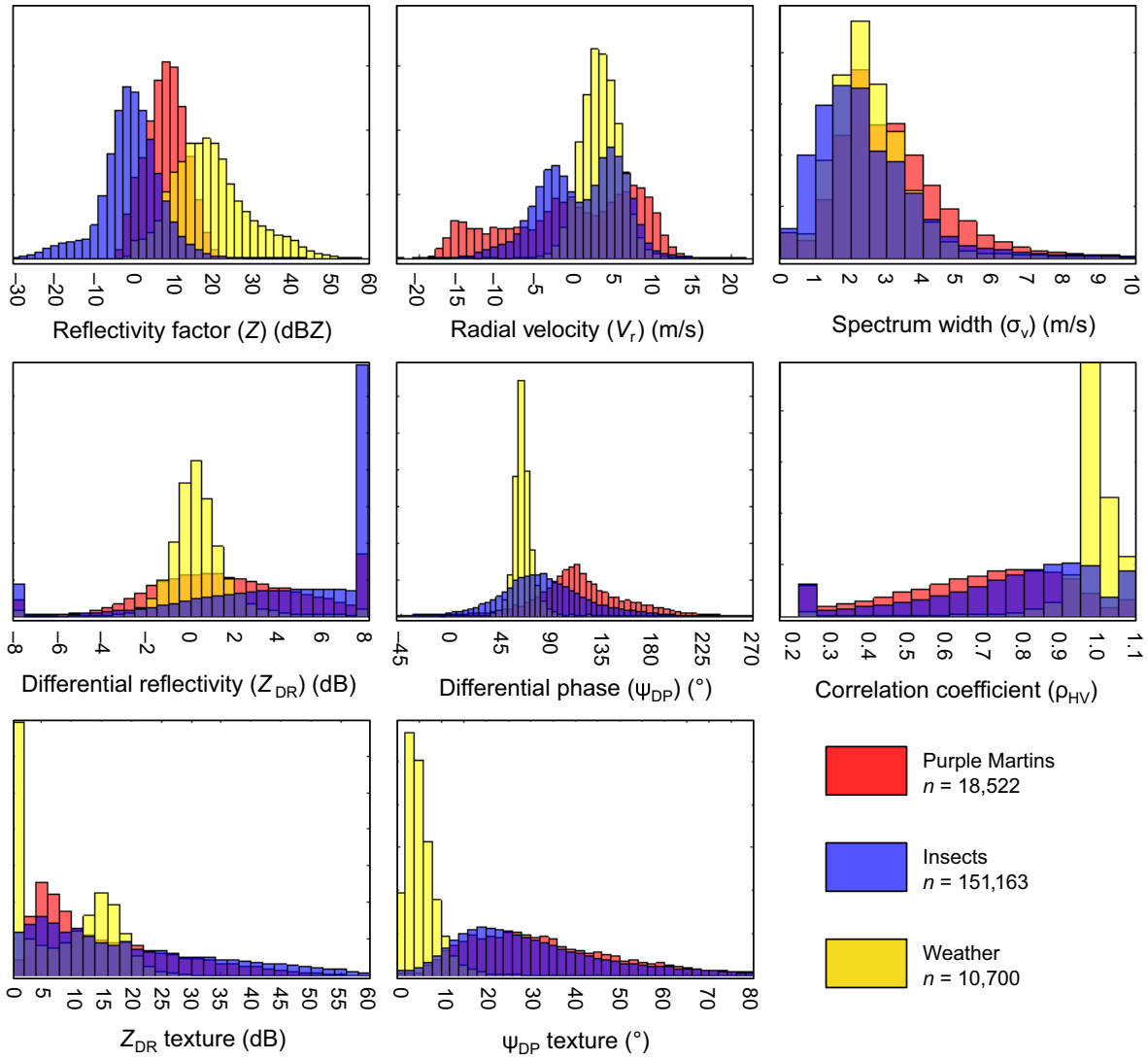

Fig. 9. Normalized frequency histograms of radar products for the three scatterer types identified in Fig. 8.

lower for weather than biological scatterers, although a second mode does occur for weather signals that corresponds with the abrupt variability at the edges of the storms. More substantially, the ψ_{DP} texture shows a clear delineation between biological and non-biological signals, with weather having much less phase variation along the radial.

Fig. 10 shows a second case for the Huntsville, Alabama radar (KHTX), on 3 May 2015 at 05:05 UTC (00:05 CDT) from the 0.5° elevation angle. All figure subplots are as described for Fig. 8. This case represents nocturnal broad front migration of birds northward in the spring, with airspeeds averaging 8.95 m/s in the lowest 2.5 km (Appendix S1). Unusually, Z_{DR} does not exhibit strong variations in azimuth, although both ρ_{HV} and ψ_{DP} do show their characteristic variability. As demonstrated by Van Den Broeke (2013) and Stepanian and Horton (2015), ρ_{HV} has symmetry across the head–tail body axis and antisymmetry across the perpendicular wing-to-wing axis. In this antisymmetric pattern, low values correspond to tail-on viewing angles and high values to head-on angles, indicating widespread headings toward the north–northeast. At present, the scattering mechanisms that result in this great variability in ρ_{HV} between head

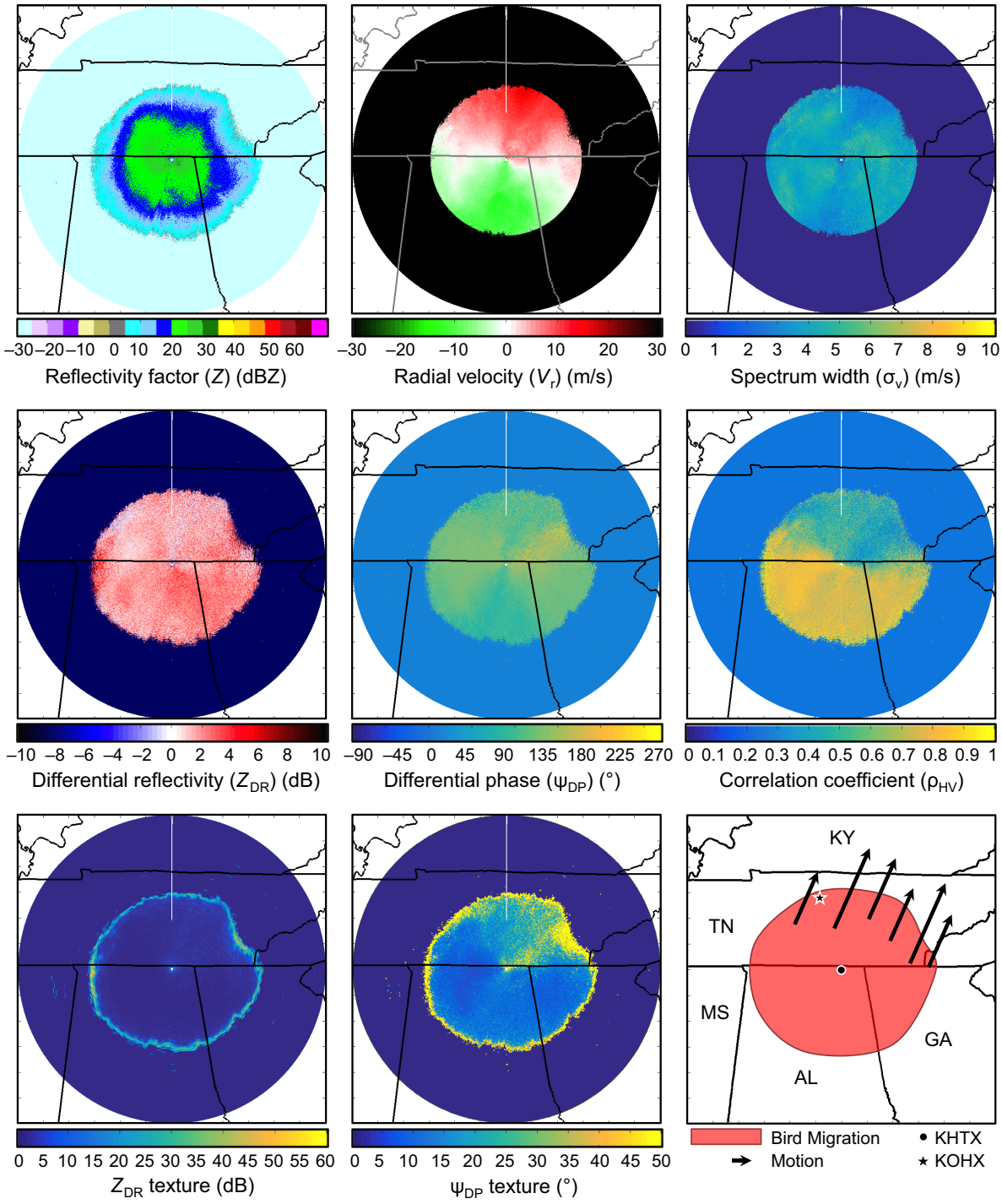

Fig. 10. Radar products for the Huntsville, Alabama NEXRAD radar (KHTX) on 3 May 2015 at 05:05 UTC for the 0.5° elevation angle. Map domain is 600 km by 600 km.

and tail view angles have not been quantified. Recalling that ρ_{HV} describes the pulse-to-pulse similarity between polarizations, it may be that bird anatomy or wing flapping has an influence on this signature, but this is only speculation. Regardless of cause, this antisymmetric pattern in ρ_{HV} during the widespread bird migration appears to be a universal signature in nocturnal avian movements across NEXRAD (Van Den Broeke 2013, Stepanian and Horton 2015, Horton et al. 2016*b*, *c*).

The polarimetric measurements presented in Figs. 8–10 are specific to the Huntsville radar, and broader observations are required to deduce general patterns and characteristic values in polarimetric fields. The differences in biological radar signatures across NEXRAD sites can be investigated by comparing simultaneous collocated observations from nearby stations. In this case, the Nashville, Tennessee NEXRAD radar (KOHX; denoted by ★) is taking overlapping measurements 152 km away to the north. Contrasting the known differences between sites, the Huntsville radar uses an operating wavelength of 10.88 cm, while the Nashville radar has a slightly shorter wavelength of 10.37 cm. Differences also exist between their initial transmission phase offsets (ψ_t), which are not measured or otherwise quantified.

Fig. 11 shows the corresponding case of nocturnal bird migration for the Nashville, Tennessee radar (KOHX) on 3 May 2015 at 05:08 UTC (00:08 CDT) from the 0.5° elevation angle. All figure subplots are as described for Figs. 8 and 10. It is likely that the species composition of the airspace is similar at both radar sites and in much of the overlapping volume it should, in fact, be identical. Despite this fact, differences exist in the measurements of the birds aloft between the two sites. Most noticeably, Z_{DR} exhibits stronger azimuthal variation, with a wedge of negative values extending to the west and a wedge of higher positive values to the southeast. Again, it is unlikely that these regions correspond with any spatial variation in flight behavior or taxonomic composition, but are purely an effect of the radar sampling process at different viewing angles with respect to the birds' heading. Furthermore, these negative values of Z_{DR} do not indicate scatterers that are larger in their vertical dimension.

Normalized frequency histograms for these two corresponding cases of nocturnal bird migration are presented in Fig. 12. While it is possible that slight taxonomic or behavioral differences may exist between these two sites, we anticipate that most of the variability is explained by differences in the radar system configurations. The distributions of reflectivity factor clearly have displaced modes, with Nashville recording lower modal values. This offset may be due to the variability in RCS with wavelength, resulting in different reflectivity factors for similar scatterers (Melnikov et al. 2012). It is also possible that this variation is due to differences in bird number concentrations aloft. Finally, imperfections in reflectivity calibration of either radar may lead to these discrepancies. The ranges of radial velocities are similar between the two distributions, while the spectrum width at Nashville is slightly broader than at Huntsville. Again, it is difficult to conclusively state whether these differences are due to the differences in radar sampling effects or flight behavior (e.g., variety in flight headings within sampling volumes).

Considering the polarimetric variables, Nashville has consistently broader distributions of all five products. Differential reflectivity has mean values of 1.8 and 1.6 dB for Huntsville and Nashville, respectively. On average, 60% of NEXRAD radars have Z_{DR} bias within 0.2 dB, and it is possible that this difference is due to imperfect system calibration. Despite Nashville having a lower Z_{DR} mean and mode, it also has more values that exceed the maximum Z_{DR} threshold, resulting in a larger spike at 8 dB. This site variability in Z_{DR} is the combined effect of the differences in wavelength, as well as the system differential phase on transmission. Additionally, this variability corresponds to higher values for the Z_{DR} texture across the Nashville site. Similarly, the distribution of differential phase is broader at the Nashville site, resulting in higher texture values of ψ_{DP}. Furthermore, because we applied a formulation of ψ_{DP} texture that was developed for meteorological scatterers, it is not designed for phase shifts that produce aliasing across the –90°/+270° transition. The large ψ_{DP} variations associated with biological scatterers result in inflated textures in regions of aliasing, such as the northeast sector at the Nashville site. For

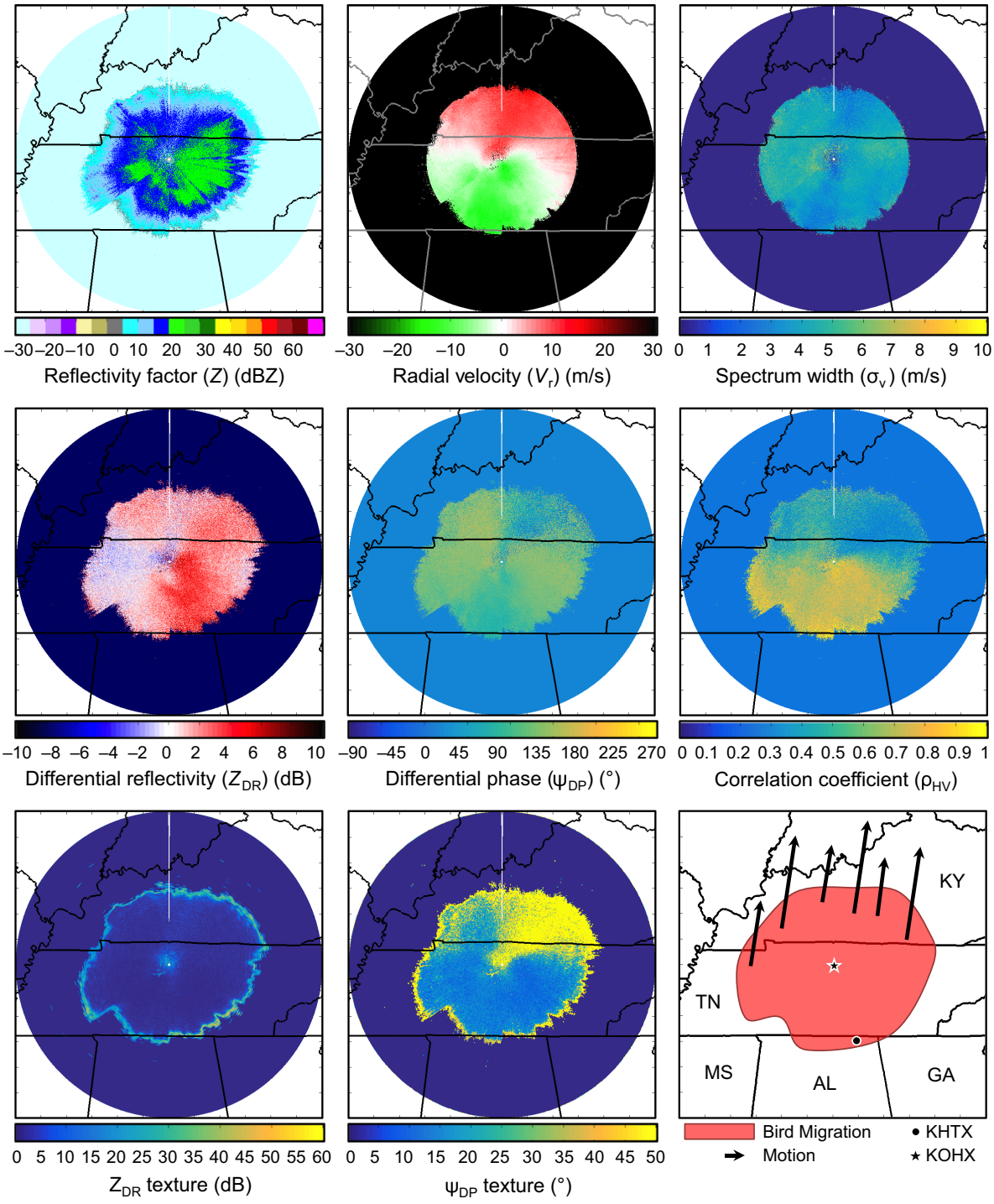

Fig. 11. Radar products for the Nashville, Tennessee NEXRAD radar (KOHX) on 3 May 2015 at 05:08 UTC for the 0.5° elevation angle. Map domain is 600 km by 600 km.

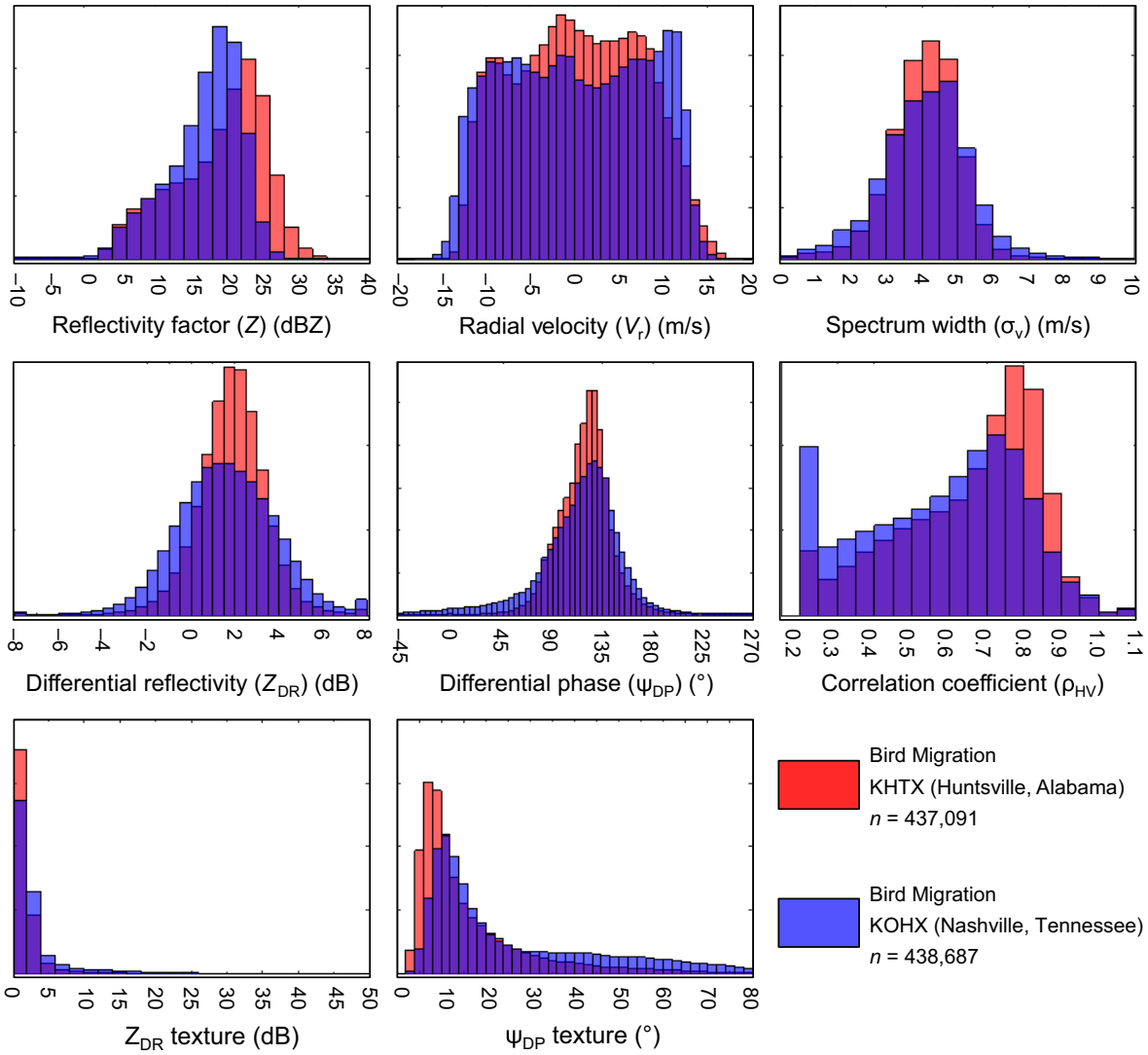

Fig. 12. Normalized frequency histograms of radar products for the fields shown in Fig. 10 (KHTX, red) and Fig. 11 (KOHX, blue). Both scans occurred at local midnight on 3 May 2015. The radar wavelengths are 10.88 cm (2755 MHz) for KHTX and 10.37 cm (2891 MHz) for KOHX.

biological applications, it would be more appropriate to use circular statistics to avoid these artifacts. Finally, there is a notable shift in the distributions of correlation coefficient between the two sites, with Nashville having lower values. For both sites, the lower tails of the ρ_{HV} distributions fall below the minimum value of 0.2, resulting in large spikes at this threshold.

A final case demonstrates an unusual effect of site-specific variability. Fig. 13 shows a snapshot of the southern United States on 19 April 2016 at 00:00 UTC (19:00 CDT on 18 April), approximately 22 min before local sunset. In this case, the classically described patterns of Z and Z_{DR} for aligned insects are present over much of the region; namely, dumb-bell patterns in both Z and Z_{DR} indicate body alignment to the north–northwest, with v_r suggesting northwestward movement (Mueller and Larkin 1985, Zrnić and Ryzhkov 1998, Lang et al. 2004, Rennie et al. 2010). Airspeed analysis using the 00 UTC Birmingham, AL, sounding on the KBMX radar yields average airspeeds of 2.39 m/s in the lowest kilometer of airspace, further supporting insect classification

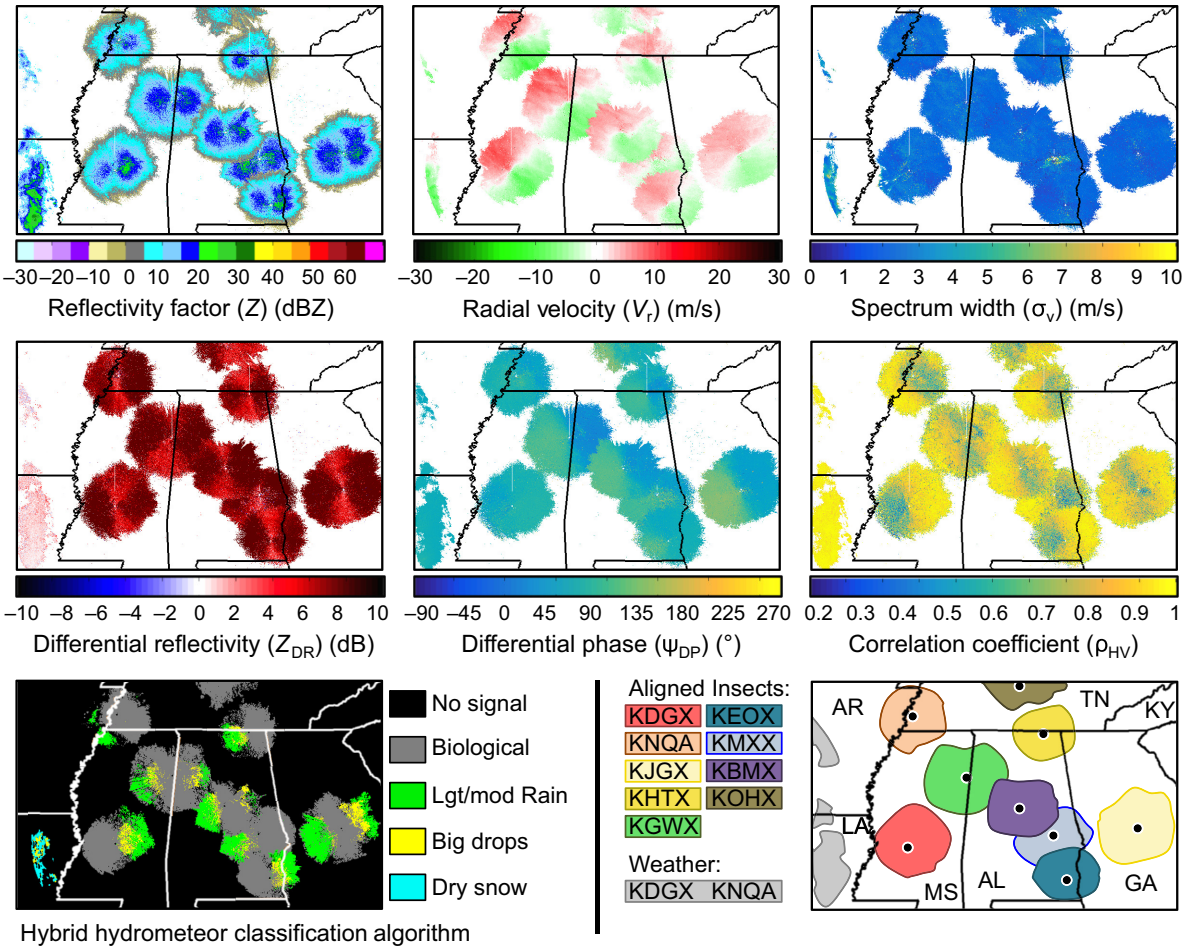

Fig. 13. Radar products across the southern United States on 19 April 2016 at 00:00 UTC for the 0.5° elevation angle. Hydrometeor classifications were obtained from the NSSL MRMS polar product site (http://mrms.ou.edu/main/legacy_polar_tools_main.html). Map domain is 1014 km by 890 km.

(Appendix S1). The annotated map of the region is presented in the bottom-right subplot, showing the widespread insect alignment over all of the radar sites, and a small swath of precipitation to the far west. While we can only speculate to the identity of these insects, it appears from the clear symmetry in Z_{DR} that resonance effects on these scatterers must be less pronounced and the magnitude of depolarization contributions may be relatively low—both of which could suggest the presence of small insects.

While Z and Z_{DR} have the expected symmetry with the head–tail body axis, both ψ_{DP} and ρ_{HV} are not symmetric across the body axis. In fact, the axis of symmetry for these products appears to be along the wing–wing axis, a result matching the observations and calculations by Melnikov et al. (2015). Perhaps more surprising is the site-to-site variability in the orientation of ρ_{HV} magnitudes. For example, KDGX and KEOX show low ρ_{HV} magnitudes on the western half of their domains (corresponding with views of the right-side wings of the insects) and high values over the eastern halves. Conversely, KNQA, KHTX, KBMX, and KMXX clearly have a reversed pattern, with high ρ_{HV} magnitudes over the western halves. The remaining sites show a third pattern with high magnitudes at both sides and a central swath of low values along the head–tail axis. The striking variability of these patterns, especially within the overlapping regions of airspace (e.g., KMXX/KEOX), indicates a cause related to

site-specific variability in the radar systems. The primary culprit could be the differential phase on transmission, which in the case of pitched insects can produce different values of ρ_{HV} and ψ_{DP} in the STAR polarimetric mode (Melnikov et al. 2015).

To illustrate a practical effect of these regions of high ρ_{HV}, the corresponding hybrid hydrometeor classification product was downloaded for each site from the Multi-Radar Multi-Sensor polar product page (http://mrms.ou.edu/main/legacy_polar_tools_main.html) and plotted over the analysis domain (Fig. 13, bottom-left). These classification products use polarimetric variables to deduce the identity of scatterers in the airspace, and often contain "biological" classes (Park et al. 2009). In this case, the widespread regions of high ρ_{HV} result in misclassification of insects as rain. Furthermore, these regions of misclassification are consistent with site-specific patterns of ρ_{HV}, demonstrating the same three morphologies. Overall, there are still many unknowns in basic interpretation of polarimetric products among NEXRAD sites, and it is clear that characterizing site-specific variability will play a major role in using these products on a broad scale.

Discussion

After more than a decade of speculation within the ecological community, the NEXRAD upgrade to operational dual polarizations has been completed. This rich data set is readily accessible and freely available, holding great potential for analyses at continental scales and time spans that are increasing by the day. But as the use of polarimetric data increases, so must our efforts in understanding the phenomena that govern these measurements. It is clear that a variety of electromagnetic and anatomical effects interact to create the final radar measurement, but a mechanistic understanding of these processes has not yet been achieved. At present, much of the work on this topic is being undertaken by radar meteorologists interested in using polarimetry to censor the cluttering signals produced by airborne animals (e.g., Chandrasekar et al. 2012, Lakshmanan et al. 2014, 2015, Tang et al. 2014, Zhang et al. 2015), and a shift in perspective is necessary to realize much of the potential for ecological applications.

The opportunities associated with polarimetric measurements are expansive, and these data are already providing new perspectives on topics in wildlife ecology (Van Den Broeke 2013, Horton et al. 2016*b*, *c*, Kelly et al. 2016, Van Doren et al. 2016). Perhaps one of the most anticipated accomplishments will be the ability to automatically identify and classify organisms by taxa—the ecological analogy to meteorologists' hydrometeor classification algorithms (Zrnić and Ryzhkov 1998, Chandrasekar et al. 2012). With it will come the capability of automated analysis of large spatial and temporal data sets for unprecedented studies on distribution, abundance, and phenology of airborne organisms (Chilson et al. 2012, Kelly and Horton 2016, Kelly et al. 2016). It does appear, however, that added nuances regarding azimuthal aspect variability and site-to-site system differences will complicate these efforts in ways that radar meteorologists typically need not consider. While these complications require a break from traditional interpretations of polarimetric variables, most notably the geometric interpretation of Z_{DR}, the meteorological literature does provide a framework for understanding these measurements. Ryzhkov and Zrnić (2007) described the theoretical basis for depolarization effects on Z_{DR} and ψ_{DP} in the presence of aligned ice crystals, and Vivekanandan et al. (1991) provided a formulation for modeling such collections of scatterers. Similar formulations have been extended to model the radar signatures of insect scatterers, accounting for system differential phase variability on transmission (Melnikov et al. 2015), as well as the variations in probing wavelength (Melnikov et al. 2012). These types of theoretical calculations will be vital to understanding how collections of organisms manifest themselves in radar measurements.

Harnessing the potential of dual-polarization measurements will largely depend on efforts to characterize the polarimetric scattering attributes of known organisms. One method for gaining this information is using geographical, environmental, or phenological knowledge to deduce the likely identity of organisms appearing in operational radar measurements. Other techniques could provide groundtruth verification of scatterers, whether in the form of organized field validation campaigns, or social or mass media reports. The potential applications of these latter

observations are becoming increasingly attractive, especially considering the high availability of photographic and video recordings from citizen scientists and other individuals. While validating the large-scale measurements is one way forward, other techniques may focus on the precise scattering characteristics of single subjects. These methods include controlled laboratory measurements of bird, bat, and insect specimens, as well as theoretical electromagnetic modeling studies of animals. In all likelihood, it will be a combination of all of these techniques that eventually yields the ability to confidently interpret the polarimetric signatures of animals aloft.

Future work will require the continued cooperation of biologists, meteorologists, computer scientists, and radar engineers to unravel the physical principles behind the correct interpretation of radio scattering from biota. Much as in the history of radar meteorology, a major step forward will come as aeroecology incorporates a classroom curriculum that includes the tools of a radar scientist. While collaboration will always be a central theme of these interdisciplinary fields, future generations of radar aeroecologists will need the skills for computing, quantitative analysis, and electromagnetics, as well as their traditional biological background. Our hope is that the work presented stimulates interest in the development of ecological polarimetric radar applications and provides the most basic interpretations of these new data products for those coming from a biological background. We also emphasize that these descriptions only scratch the surface of the topic, and a vast body of existing literature expands upon these concepts (Bringi and Chandrasekar 2001). As the field continues to develop, it will be the continued investment in education and basic research that ultimately yields sophisticated analyses, applications, and monitoring systems for conservation and ecological studies.

Acknowledgments

This work was supported by the Marshall Sherfield Fellowship and NSF Grant EF-1340921. We would like to thank the University of Oklahoma Aeroecology Group, as well as the attendees of the radar ornithology workshop and symposium at the 2015 meeting of the American Ornithologists' Union and Cooper Ornithological Society, for their insightful discussions that strengthened this manuscript. Additionally, we thank two anonymous reviewers for their constructive comments, and Charlotte Wainwright for her technical edits on this manuscript.

Literature Cited

Bonter, D. N., S. A. Gauthreaux Jr., and T. M. Donovan. 2009. Characteristics of important stopover locations for migrating birds: remote sensing with radar in the Great Lakes basin. Conservation Biology 23:440–448.

Bridge, E. S., S. M. Pletschet, T. Fagin, P. B. Chilson, K. G. Horton, K. R. Broadfoot, and J. F. Kelly. 2015. Persistence and habitat associations of purple martin roosts quantified via weather surveillance radar. Landscape Ecology 31:43–53.

Bringi, V. N., and V. Chandrasekar. 2001. Polarimetric Doppler weather radar: principles and applications. First edition. Cambridge University Press, Cambridge, UK.

Buler, J. J., and D. K. Dawson. 2014. Radar analysis of fall bird migration stopover sites in the northeastern U.S. Condor 116:357–370.

Buler, J. J., and R. H. Diehl. 2009. Quantifying bird density during migratory stopover using weather surveillance radar. IEEE Transactions on Geoscience and Remote Sensing 47:2741–2751.

Buler, J. J., L. A. Randall, J. P. Fleskes, W. C. Barrow Jr., T. Bogart, and D. Kluver. 2012. Mapping wintering waterfowl distributions using weather surveillance radar. PLoS ONE 7:1–9.

Chandrasekar, V., R. Keränen, S. Lim, and D. Moisseev. 2012. Recent advances in classification of observations from dual polarization weather radars. Atmospheric Research 119:97–111.

Chilson, P. B., W. F. Frick, J. F. Kelly, K. W. Howard, R. P. Larkin, R. H. Diehl, J. K. Westbrook, T. A. Kelly, and T. H. Kunz. 2012. Partly cloudy with a chance of migration: weather, radars, and aeroecology. Bulletin of the American Meteorological Society 93:669–686.

Cleveland, C., et al. 2006. Economic value of the pest control service provided by Brazilian free-tailed bats in south-central Texas. Frontiers in Ecology and the Environment 4:238–243.

Crum, T. D., R. L. Alberty, and D. W. Burgess. 1993. Recording, archiving, and using WSR-88D data. Bulletin of the American Meteorological Society 74:645–653.

Diehl, R. H., and R. P. Larkin. 2005. Introduction to the WSR-88D (NEXRAD) for ornithological research. Pages 878–290 *in* C. J. Ralph and T. D. Rich, editors. Bird Conservation Implementation and Integration

in the Americas: Proceedings of the Third International Partners in Flight Conference, Asilomar, Pacific Grove, California, USA, March 20–24, 2002. U.S. Department of Agriculture, Forest Service, Albany, California, USA.

Diehl, R. H., R. P. Larkin, and J. E. Black. 2003. Radar observations of bird migration over the Great Lakes. Auk 120:278–290.

Doviak, R. J., V. Bringi, A. Ryzhkov, A. Zahrai, and D. Zrnić. 2000. Considerations for polarimetric upgrades to operational WSR-88D radars. Journal of Atmospheric and Oceanic Technology 17:257–278.

Doviak, R. J., and D. S. Zrnić. 1993. Doppler radar and weather observations. Second edition. Academic Press (reprinted in 2006 by Dover Publications Inc., Mineola, New York, USA).

Drake, V. A., and D. R. Reynolds. 2012. Radar entomology: observing insect flight and migration. CABI, Wallingford, UK.

Eastwood, E. 1967. Radar ornithology. Methuen & Co., London, UK.

Fang, M., R. J. Doviak, and V. Melnikov. 2004. Spectrum width measured by WSR-88D: error sources and statistics of various weather phenomena. Journal of Atmospheric and Oceanic Technology 21:888–904.

Farnsworth, A., S. A. Gauthreaux Jr., and D. E. Van Blaricom. 2004. A comparison of nocturnal call counts of migrating birds and reflectivity measurements on Doppler radar. Journal of Avian Biology 35: 365–369.

Farnsworth, A., B. M. Van Doren, W. M. Hochachka, D. Sheldon, K. Winner, J. Irvine, J. Geevarghese, and S. Kelling. 2016. A characterization of autumn nocturnal migration detected by weather surveillance radars in the northeastern US. Ecological Applications 26:752–770.

Frick, W. F., P. M. Stepanian, J. F. Kelly, K. W. Howard, C. M. Kuster, T. H. Kunz, and P. B. Chilson. 2012. Climate and weather impact timing of emergence of bats. PLoS ONE 7:1–8.

Gauthreaux Jr., S. A. 1971. A radar and direct visual study of passerine spring migration in southern Louisiana. Auk 88:343–365.

Gauthreaux Jr., S. A., and C. G. Belser. 1998. Displays of bird movements on the WSR-88D: patterns and quantification. Weather and Forecasting 13: 453–464.

Gauthreaux Jr., S. A., J. W. Livingston, and C. G. Belser. 2008. Detection and discrimination of fauna in the aerosphere using Doppler weather surveillance radar. Integrative and Comparative Biology 48: 12–23.

Gourley, J. J., P. Tabary, and J. Parent du Chatelet. 2007. A fuzzy logic algorithm for the separation of precipitating from nonprecipitating echoes using polarimetric radar observations. Journal of Atmospheric and Oceanic Technology 24:1439–1451.

Horn, J. W., and T. H. Kunz. 2008. Analyzing NEXRAD Doppler radar images to assess nightly dispersal patterns and population trends in Brazilian free-tailed bats (*Tadarida Brasiliensis*). Integrative and Comparative Biology 48:24–39.

Horton, K. G., W. G. Shriver, and J. J. Buler. 2015. A comparison of traffic estimates of nocturnal flying animals using radar, thermal imaging, and acoustic recording. Ecological Applications 25: 390–401.

Horton, K. G., W. G. Shriver, and J. J. Buler. 2016*a*. An assessment of spatio-temporal relationships between nocturnal bird migration traffic rates and diurnal bird stopover density. Movement Ecology 4:1–10.

Horton, K. G., B. M. Van Doren, P. M. Stepanian, A. Farnsworth, and J. F. Kelly. 2016*b*. Seasonal differences in landbird migration strategies. Auk 133:761–769.

Horton, K. G., B. M. Van Doren, P. M. Stepanian, W. M. Hochachka, A. Farnsworth, and J. F. Kelly. 2016*c*. Nocturnally migrating songbirds drift when they can and compensate when they must. Scientific Reports 6:1–8.

Kelly, J. F., and K. G. Horton. 2016. Toward a predictive macrosystems framework for migration ecology. Global Ecology and Biogeography 25:1159–1165.

Kelly, J. F., K. G. Horton, P. M. Stepanian, K. de Beurs, T. Fagin, E. S. Bridge, and P. B. Chilson. 2016. Novel measures of continental-scale avian migration phenology related to proximate environmental cues. Ecosphere 7:1–13.

Kelly, J. F., J. R. Shipley, P. B. Chilson, K. W. Howard, W. F. Frick, and T. H. Kunz. 2012. Quantifying animal phenology in the aerosphere at a continental scale using NEXRAD weather radars. Ecosphere 3:1–9.

Kumjian, M. R. 2013*a*. Principles and applications of dual-polarization weather radar. Part I: description of the polarimetric radar variables. Journal of Operational Meteorology 1:226–242.

Kumjian, M. R. 2013*b*. Principles and applications of dual-polarization weather radar. Part II: warm and cold season applications. Journal of Operational Meteorology 1:243–264.

Kumjian, M. R. 2013*c*. Principles and applications of dual-polarization weather radar. Part III: artifacts. Journal of Operational Meteorology 1:265–274.

Lafleur, J. M., J. J. Buler, and F. R. Moore. 2016. Geographic position and landscape composition explain regional patterns of migrating landbird distributions during spring stopover along the

northern coast of the Gulf of Mexico. Landscape Ecology 31:1697–1709.

Lakshmanan, V., C. Karstens, J. Krause, K. Elmore, A. Ryzhkov, and S. Berkseth. 2015. Which polarimetric variables are important for weather/no-weather discrimination? Journal of Atmospheric and Oceanic Technology 32:1209–1223.

Lakshmanan, V., C. Karstens, J. Krause, and L. Tang. 2014. Quality control of weather radar data using polarimetric variables. Journal of Atmospheric and Oceanic Technology 31:1234–1249.

Lang, T. J., S. A. Rutledge, and J. L. Stith. 2004. Observations of quasi-symmetric echo patterns in clear air with the CSU-CHILL polarimetric radar. Journal of Atmospheric and Oceanic Technology 21:1182–1189.

Larkin, R. P., and R. H. Diehl. 2012. Radar techniques for wildlife research. Pages 319–335 *in* N. J. Silvy, editor. The wildlife techniques manual. Seventh edition. The Johns Hopkins University Press, Baltimore, Maryland, USA.

La Sorte, F. A., W. M. Hochachka, A. Farnsworth, D. Sheldon, D. Fink, J. Geevarghese, K. Winner, B. M. Van Doren, and S. Kelling. 2015*a*. Migration timing and its determinants for nocturnal migratory birds during autumn migration. Journal of Animal Ecology 84:1202–1212.

La Sorte, F. A., W. M. Hochachka, A. Farnsworth, D. Sheldon, B. M. Van Doren, D. Fink, and S. Kelling. 2015*b*. Seasonal changes in the altitudinal distribution of nocturnally migrating birds during autumn migration. Royal Society Open Science 2:1–13.

Liu, S., Q. Xu, and P. Zhang. 2005. Identifying Doppler velocity contamination caused by migrating birds. Part II: Bayes identification and probability tests. Journal of Atmospheric and Oceanic Technology 22:1114–1121.

Martin, W. J., and A. Shapiro. 2007. Discrimination of bird and insect radar echoes in clear air using high-resolution radars. Journal of Atmospheric and Oceanic Technology 24:1215–1230.

McCracken, G. F., E. H. Gillam, J. K. Westbrook, Y. Lee, M. L. Jensen, and B. B. Balsley. 2008. Brazilian free-tailed bats (*Tadarida Brasiliensis*: Molossidae, Chiroptera) at high altitude: links to migratory insect populations. Integrative and Comparative Biology 48:107–118.

Melnikov, V. M., M. J. Istok, and J. K. Westbrook. 2015. Asymmetric radar echo patterns from insects. Journal of Atmospheric and Oceanic Technology 32:659–674.

Melnikov, V. M., R. R. Lee, and N. J. Langlieb. 2012. Resonance effects within S-band in echoes from birds. IEEE Geoscience and Remote Sensing Letters 9:413–416.

Mie, G. 1908. Beiträge Zur Optik Trüber Medien, Speziell Kolloidaler Metallösungen. Anngeo 25:377–445.

Mueller, E. A., and R. P. Larkin. 1985. Insects observed using dual-polarization radar. Journal of Atmospheric and Oceanic Technology 2:49–54.

O'Neal, B. J., J. D. Stafford, and R. P. Larkin. 2010. Waterfowl on weather radar: applying ground-truth to classify and quantify bird movements. Journal of Field Ornithology 81:71–82.

O'Neal, B. J., J. D. Stafford, and R. P. Larkin. 2014. Migrating ducks in inland North America ignore major rivers as leading lines. Ibis 157:154–161.

Park, H., A. V. Ryzhkov, D. S. Zrnić, and K. Kim. 2009. The hydrometeor classification algorithm for the polarimetric WSR-88D: description and application to an MCS. Weather and Forecasting 24: 730–748.

Rennie, S. J., A. J. Illingworth, S. L. Dance, and S. P. Ballard. 2010. The accuracy of Doppler radar wind retrievals using insects as targets. Meteorological Applications 17:419–432.

Rinehart, R. E. 2010. Radar for meteorologists. Fifth edition. Rinehart Publications, Nevada, Missouri, USA.

ROC. 2014. Initial system differential phase offset/correction, ST22. NOAA Radar Operations Center, Norman, Oklahoma, USA. http://www.roc.noaa.gov/wsr88d/PublicDocs/DualPol/PossibleImpactsduetoIncorrectISDP.pdf

Russell, K. R., and S. A. Gauthreaux Jr. 1998. Use of weather radar to characterize movements of roosting purple martins. Wildlife Society Bulletin 26:5–16.

Ruth, J. M., R. H. Diehl, and R. K. Felix Jr. 2012. Migrating birds' use of stopover habitat in the southwestern Unites States. Condor 114:698–710.

Ryzhkov, A. V. 2007. The impact of beam broadening on the quality of radar polarimetric data. Journal of Atmospheric and Oceanic Technology 24:729–744.

Ryzhkov, A. V., T. J. Schuur, D. W. Burgess, P. L. Heinselman, S. E. Giangrande, and D. S. Zrnic. 2005. The joint polarization experiment: polarimetric rainfall measurements and hydrometeor classification. Bulletin of the American Meteorological Society 86:809–824.

Ryzhkov, A. V., and D. S. Zrnić. 2007. Depolarization in ice crystals and its effect on radar polarimetric measurements. Journal of Atmospheric and Oceanic Technology 24:1256–1267.

Sachidananda, M., and D. S. Zrnić. 1985. Z_{DR} measurement considerations for a fast scan capability radar. Radio Science 20:907–922.

Sheldon, D., A. Farnsworth, J. Irvine, B. M. Van Doren, K. Webb, T. G. Dietterich, and S. Kelling. 2013.

Approximate Bayesian inference for reconstructing velocities of migrating birds from weather radar. Pages 1334–1340 *in* Proceedings of the Twenty-Seventh AAAI Conference on Artificial Intelligence, Bellevue, Washington, USA, July 14–18, 2013. Association for the Advancement of Artificial Intelligence, Palo Alto, California, USA.

Stepanian, P. M. 2015. Radar Polarimetry for Biological Applications. Dissertation. University of Oklahoma, Norman, Oklahoma, USA.

Stepanian, P. M., and K. G. Horton. 2015. Extracting migrant flight orientation profiles using polarimetric radar. IEEE Transactions on Geoscience and Remote Sensing 53:6518–6528.

Tang, L., J. Zhang, C. Langston, J. Krause, K. Howard, and V. Lakshmanan. 2014. A physically based precipitation-nonprecipitation radar echo classifier using polarimetric and environmental data in a real-time national system. Weather and Forecasting 29:1106–1119.

Van Den Broeke, M. S. 2013. Polarimetric radar observations of biological scatterers in Hurricanes Irene (2011) and Sandy (2012). Journal of Atmospheric and Oceanic Technology 30:2754–2767.

Van Doren, B. M., K. G. Horton, P. M. Stepanian, D. S. Mizrahi, and A. Farnsworth. 2016. Wind drift explains the reoriented morning flights of songbirds. Behavioral Ecology 27:1122–1131.

Van Doren, B. M., D. Sheldon, J. Geevarghese, W. M. Hochachka, and A. Farnsworth. 2015. Autumn morning flights of migrant songbirds in the northeastern United States are linked to nocturnal migration and winds aloft. Auk 132:105–118.

Vivekanandan, J., W. M. Adams, and V. N. Bringi. 1991. Rigorous approach to polarimetric radar modeling of hydrometeor orientation distributions. Journal of Applied Meteorology 30:1053–1063.

Westbrook, J. K. 2008. Noctuid migration in Texas within the nocturnal aeroecological boundary layer. Integrative and Comparative Biology 48: 99–106.

Westbrook, J. K., R. S. Eyster, and W. W. Wolf. 2013. WSR-88D Doppler radar detection of corn earworm moth migration. International Journal of Biometeorology 58:931–940.

Zhang, J., et al. 2015. Multi-radar multi-sensor (MRMS) quantitative precipitation estimation: initial operating capabilities. Bulletin of the American Meteorological Society 97:621–638.

Zhang, P., S. Liu, and Q. Xu. 2005. Identifying Doppler velocity contamination caused by migrating birds. Part I: feature extraction and quantification. Journal of Atmospheric and Oceanic Technology 22:1105–1113.

Zrnić, D. S., V. M. Melnikov, and A. V. Ryzhkov. 2006. Correlation coefficients between horizontally and vertically polarized returns from ground clutter. Journal of Atmospheric and Oceanic Technology 23:381–394.

Zrnić, D. S., and A. V. Ryzhkov. 1998. Observations of insects and birds with a polarimetric radar. IEEE Transactions on Geoscience and Remote Sensing 36:661–668.

Zrnić, D. S., and A. V. Ryzhkov. 1999. Polarimetry for weather surveillance radars. Bulletin of the American Meteorological Society 80:389–406.

Supporting Information

Additional Supporting Information may be found online at: http://onlinelibrary.wiley.com/doi/10.1002/ecs2.1539/full